TECHNISCHE UNIVERSITÄT WIEN
Vienna University of Technology

DIPLOMARBEIT

Optics Design for the Low Luminosity Experiments in the FCC-hh

Ausgeführt am Atominstitut
der Technischen Universität Wien
unter der Anleitung von
Privatdoz. Dipl.-Ing Dr.techn **Michael Benedikt**
Dr. **Rogelio Tomás Garcia**

durch
Michael Hofer
Schlossee 1 / 229
2522 Oberwaltersdorf

Genf, September 2017

Abstract

Following the recommendation of the European Strategy Group for Particle Physics, the Future Circular Collider (FCC) study was launched by CERN to investigate circular collider designs for a post-LHC era. Among the studied collider designs is a hadron-collider option aiming to collide proton at a center of mass energy of 100 TeV. This hadron collider option (FCC-hh) follows a similar layout as the LHC with two high luminosity experimental insertions, meant to complement each other and two low luminosity experiments. This thesis studies the option of combining these low luminosity experiments with the injection in the FCC-hh. Using a contrary design approach to the combined insertion in the LHC and taking into account the constraint from the injection a layout was developed. The goal when developing the beam optics for the insertion was to achieve the lowest possible beam size in the interaction point to guarantee a high event rate. Furthermore, the impact of magnetic field errors in the magnets of this insertion on the beam stability was studied and are discussed in this thesis. In addition, a possible strategy is then presented which would allow to further increase the event rate.

Contents

CHAPTER 1

Introduction

Since the first particle collider was built and operated in the mid 20th century they proved to be an invaluable tool to study subatomic particles. Over time colliders did not only grow in size and achieved ever increasing collision energies but also the understanding on how to operate and optimize the performance of these complex machines got better allowing substantial advancements in high energy physics (HEP).
The current pinnacle of this development is the Large Hadron Collider (LHC) located at CERN (European Organization for Nuclear Research), the world's largest and most powerful particle collider. It allows studying the validity of the standard model as well as helping to answer some of the fundamental open questions in physics at currently unrivaled collision energies and rates. One of the most significant scientific discoveries made possible by the LHC was the discovery of the Higgs Boson, often regarded as the missing puzzle piece in the standard model. Still many fundamental questions in physics like dark matter or the existence of supersymmetric partner to the standard model particles remain yet unanswered. To further enhance the discovery potential of the LHC a major upgrade, the High Luminosity LHC (HL-LHC), is planned for 2020 to further increase the collision rate.
The Future Circular Collider (FCC) study, launched by CERN in 2014 following recommendations of the European Strategy Group for Particle Physics, investigates even more powerful circular collider options for a post-LHC era with a higher discovery potential. One option studied is the construction of a new, larger hadron collider, the FCC-hh, aiming to increase the center of mass energy by a factor 7 compared to the LHC. For the experiments in the FCC-hh not only the increased collision energy is of great importance but also the minimum beam size achieved by the focusing system as it defines the attainable event rate.
This is the main goal of optics design, taking into account various constraints coming from e.g. magnet design, radiation protection, and cryogenics and designing the experimental insertion in such a way that it provides optimal conditions for the experiments. This thesis focuses on the optics design of the low luminosity experimental insertions

for the FCC-hh. Similar to the LHC, these insertions house not only experiments but it is also here where the beam coming from a preaccelerator will be injected. The challenges and main considerations when designing such a combined insertion will be one of the main points of this thesis. After introducing the FCC-study, its components and main goals in Chapter 2, Chapter 3 gives a short introduction to accelerator beam physics relevant when designing such an insertion as well as the used tools.

Chapter 4 focuses on the building blocks of an experimental and injection insertions for particle colliders.

In Chapter 5 first designs of this combined experimental and injection insertion are presented together with the achieved minimum beam size in the interaction point.

Dynamic aperture studies for magnetic errors in the low luminosity insertions are discussed in Chapter 6.

Finally, in Chapter 7 a summary of the project is presented together with possible future steps.

CHAPTER 2

Future Circular Collider Study

The discovery of the Higgs Boson 2012 by the two experimental collaboration ATLAS and CMS [1, 2] at the LHC at CERN completed the standard model of particle physics. However, there are still some fundamental questions which are yet unanswered. To this point, the capabilities of LHC will need to be fully exploited and together with its high luminosity upgrade HL-LHC will prove to be an unrivaled tool to study concepts like supersymmetry or dark matter. Yet fully studying these topics might lie beyond the (HL-)LHC capabilities.

To study physics beyond the standard model with particle colliders two different approaches are imaginable. The first approach would be to go for more precise measurements of the Higgs Boson and its decay modes. Due to the low background in electron-positron colliders these are favored for Higgs physics.

The second possibility is to push the collision energy further to search for new, heavy particles lying beyond the current energy reach of existing colliders. Due to the higher attainable energy these so-called discovery machines usually collide hadrons. The LHC is one such discovery machine achieving record center of mass collision energies for both protons and lead-ions.

Future Collider studies on both of these fronts can, in general, be split into linear collider studies and circular collider studies. On the linear collider front, the Compact Linear Collider (CLIC) study [3] and the International Linear Collider (ILC) project [4] aim to operate at energies up to the TeV range, higher than any existing electron-positron collider.

The Future Circular Collider study (FCC) on the other hand explores possible circular collider designs as a next step after the HL-LHC. The study was launched in 2014 following the recommendations of the European Strategy Group for Particle Physics [5] under the leadership of CERN and under the auspices of the European Committee for Future Accelerators (ECFA). As a global collaboration, it combines efforts of 111 institutes and laboratories from 32 countries. The various options studied in the FCC-study will be described in further detail in the following.

2.1 FCC-hh

The FCC-hh is a proposed proton-proton collider aiming to push the energy frontier to unprecedented levels by colliding particles with a center of mass energy of 100 TeV, about 7 times higher than the currently most powerful collider, the LHC with a design center of mass energy of 14 TeV [6]. This collider would be hosted in a tunnel in the Geneva basin with a circumference close to 100 km allowing to be connected to the CERN accelerator chain for using it as an injector. This is illustrated in Figure 2.1a. One of the main focus of the study is the development of dipole with a magnetic field of 16 T, almost double of the current LHC dipole field, to allow such high beam energies in the available space. The energy of 8 GJ stored in each FCC beam poses serious challenges for collimation, machine protection, and beam disposal in order to avoid magnet quenches and destruction of accelerator equipment. For example, the energy of one single bunch could already be sufficient to cause serious damage to absorber materials currently used in the LHC [7]. Compared to LHC the emitted synchrotron radiation power of 2.4 MW is also not negligible anymore. To efficiently channel the synchrotron radiation a new beam screen was designed for the FCC-hh.
The latest overall layout of the FCC-hh is similar to the LHC layout with two general purpose, high luminosity experiments hosted in opposing Interaction regions (Points A and G in Figure 2.1b) as well as two low-luminosity experimental insertions (Points B and L in Figure 2.1b), where also the injection of the beam will take place. The FCC-hh is not only designed to collide at record energies but also aims to achieve the same peak luminosity in the high luminosity experiments of $5 \cdot 10^{34}\mathrm{cm}^{-1}\mathrm{s}^{-1}$ in the baseline scenario as the HL-LHC and outperform it by a factor 6 in the ultimate scenario. The envisaged beam parameters relevant to achieving this luminosity levels are presented in Table 2.1. Furthermore, the option to collide ions in the FCC-hh is also investigated [8].

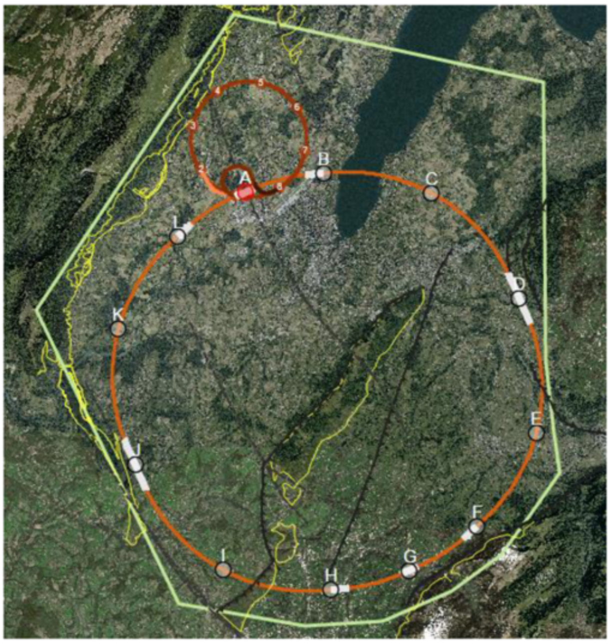

(a) Illustration of a possible location for the FCC-hh ring in the Geneva Basin [9]

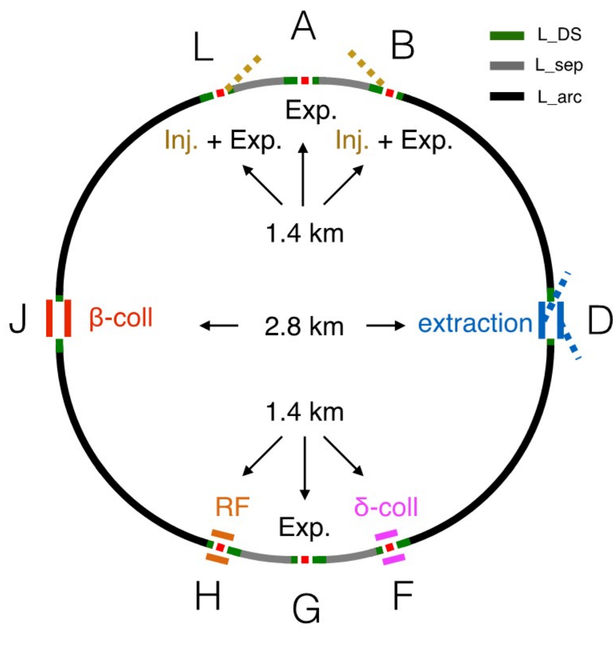

(b) Current layout of FCC-hh [10]

Figure 2.1: Illustrations of the location and layout of FCC-hh

	LHC Design	HL-LHC	HE-LHC	FCC-hh Baseline (Ultimate)
Center of mass energy [TeV]	14	14	27	100
Circumference C [km]	26.7	26.7	26.7	100
Dipole Field [T]	8.33	8.33	16	16
Number of IPs	2+2	2+2	2+2	2+2
Injection Energy [TeV]	0.45	0.45	0.45	3.3
Peak luminosity in the high luminosity experiments [10^{34}cm^{-1}s^{-1}]	1	5	25	5 ($<$ 30)
Peak no. of inelastic events/crossing	27	135 (lev.)	800	171 (1026)
Number of bunches n	2808	2808	-	10600
Bunch population N [10^{11}]	1.15	2.2	2.2	1.0
Nominal transverse normalized emittance	3.75	2.5	2.5	2.2
Maximum beam-beam tune-shift	0.01	0.015	-	0.01 (0.03)
Beam current [A]	0.584	1.12	1.12	0.5
Stored energy per beam [GJ]	0.392	0.694	1.3	8.4
Synchrotron Radiation power per ring [MW]	0.0036	0.0073	0.101	2.4
Arc Synchrotron radiation heat load [W/m/aperture]	0.17	0.33	4.6	28.4
Energy loss per turn [MeV]	0.0067	0.0067	0.093	4.6

Table 2.1: FCC-hh Key parameter compared to LHC, HL-LHC, and HE-LHC [11, 12]

2.2 FCC-he

The FCC-he study investigates a possible proton-electron collider configuration to further study deep inelastic scattering. Present considerations suggest that one of the low luminosity interaction regions of the FCC-hh could be used to collide one of the 50 TeV proton beam from the FCC-hh with a 60 GeV electron beam coming from an energy recovery linear accelerator [13]. The operation of this experiment is envisaged to work alongside the high luminosity experiments of the FCC-hh.

2.3 HE-LHC

Part of the Future Circular Study is also the option to increase the beam energy of the LHC by using the 16 T dipole technology studied for the FCC-hh. The use of those dipoles would allow going to a center of mass energy of 27 TeV, almost double compared to the LHC, while significantly cutting the cost due to the preexisting tunnel. The targeted peak luminosity of the high luminosity insertions is four times higher compared to the HL-LHC [12].

2.4 FCC-ee

A high precision option is also being investigated in the FCC study which can precede the hadron collider option. The FCC-ee, a positron-electron collider, is envisaged to be hosted in the same tunnel as its eventual successor, the FCC-hh. Although the beam energy is severely limited in circular lepton colliders due to significant synchrotron radiation losses they can provide a significantly higher collision rate compared to linear colliders [14]. The energy range of the FCC-ee, though rather limited compared to linear colliders like ILC and CLIC, allows precision tests at [15]

- the Z-Pole with $\sqrt{s} = 90\text{GeV}$ to allow high precision measurements of M_Z and Γ_Z and searches for rare decays
- the WH pair production threshold at $\sqrt{s} = 160\text{GeV}$ for precision measurements of M_W
- the ZH production mode ($\sqrt{s} = 240\text{GeV}$) where Higgs Boson production rate is at its highest allowing precise studies of the Higgs Boson
- the $t\bar{t}$ threshold ($\sqrt{s} = 350\text{GeV}$) or above it to allow precision measurement of the top quark

	LEP2	FCC-ee				
Circumference [km]	26.7	100				
energy/beam [GeV]	105	45.6		80	120	175
bunches/beam	4	30180	91500	5260	770	78
beam current [mA]	3	1450		152	30	6.6
luminosity / IP [$10^{34}\mathrm{cm}^{-1}\mathrm{s}^{-1}$]	0.0012	207	90	19	5.1	1.3
energy loss / turn [GeV]	3.34	0.03		0.3	1.67	7.55
total synchrotron radiation power [MW]	22	100	100	100	100	100
rms horizontal emittance ϵ_x [nm]	22	0.2	0.1	0.26	0.6	1.3
rms horizontal emittance ϵ_y [pm]	250	1	1	1	1	2.5

Table 2.2: FCC-ee Key parameter compared to those achieved in LEP2 [15]

Running this collider with four different energies without major modifications requires a very flexible lattice and thorough optimization for the different beam parameter of the respective energy, some of which are presented in Table 2.2. In addition, due the emitted high powered synchrotron radiation a highly optimized absorber design is required to protect machine elements.

CHAPTER 3

Accelerator and Beam Physics

In this chapter, a brief introduction to the basic concepts of beam dynamics is given. Special focus is put on the derivation of a mechanism to describe the oscillation amplitude of many particles in a bunch by an envelope function. Thereafter this mechanism is extended to particles with a deviation from the reference momentum and include also the treatment of beam in the presence of misaligned elements. The chapter closes with the introduction of the used tools to simulate large-scale projects like the LHC or the FCC-hh.

3.1 Coordinate System

To describe the motion of particles in a circular accelerator it is convenient to describe the particle trajectory using a right-handed curvilinear coordinate system (x,y,s). Here the coordinate s is tangent to the reference orbit and is the longitudinal position in the accelerator. The coordinates x and y refer to the axes perpendicular to s where x is usually in the bending plane. With this choice of coordinate system, all particles in the accelerator are described by the displacement with respect to the reference orbit. Usually, in particle accelerators, the motion of a particle in the three axes can in first-order be decoupled. The study of the motion in the s-axis is called longitudinal beam dynamics whereas the study of the motion in the transverse plane is fittingly called transverse beam dynamics.

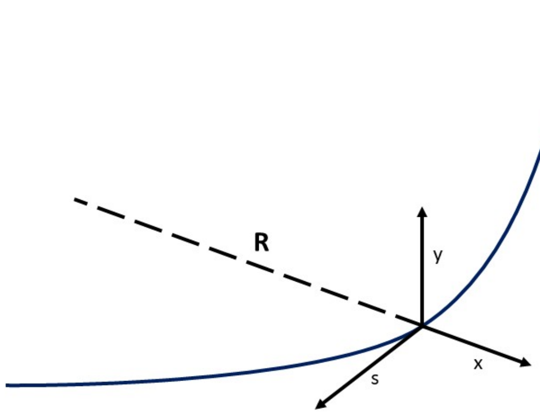

Figure 3.1: Coordinate system commonly used for describing accelerators. x and y describe the transverse offset from the reference orbit whereas s is the longitudinal position in the accelerator.

3.2 Lorentz Force

In particle accelerators, the force guiding particles with the charge q on its trajectory is the Lorentz force

$$\frac{d\vec{p}}{dt} = \vec{F} = q\left(\vec{E} + \vec{v} \times \vec{B}\right), \tag{3.1}$$

where $\vec{E}$ is the electrical field, $\vec{v}$ the velocity of the particle and $\vec{B}$ the magnetic field. From

$$\Delta E = \int_{\vec{r}_1}^{\vec{r}_2} \vec{F} \cdot d\vec{r} = \int_{\vec{r}_1}^{\vec{r}_2} q\left(\vec{E} + \vec{v} \times \vec{B}\right) \cdot d\vec{r} \tag{3.2}$$

it can be seen that since velocity $\vec{v}$ is always parallel to the path element $d\vec{r}$, acceleration of the particle can only be achieved using electric fields. Nevertheless, magnetic fields are of great importance too as they are needed for steering the particle beam. For example, for relativistic particles ($v \simeq c$) the equivalent of a magnetic field of $B = 1\ T$ would be an electric field of $E = 3 \cdot 10^8\ Vm^{-1}$ whereas the currently achievable field is below $10^7\ V/m^{-1}$ [16].

For a circular orbit and in the absence of other fields except for a dipole field the Lorentz force must be equal to the inertial force, which yields

$$B\rho = \frac{p}{q}, \tag{3.3}$$

where B is the magnetic field strength in the axis perpendicular to the bending plane, ρ the bending radius, p the particle momentum and q the charge of the particle. The term $B\rho$ is called the beam rigidity and is a measure of how difficult it is to bend the beam. Equation (3.3) shows that when the particle energy increases the magnetic field also needs to increase accordingly in order to ensure a constant bending radius. In fact, the name synchrotron derives from synchronously increasing the magnetic field with the particle energy.

3.3 Equation of motion

In the vicinity of the design orbit the magnetic field can be expanded into a series of multipoles which yields

$$\begin{aligned}\frac{q}{p}B_y(x) &= \frac{q}{p}B_{y0} \quad +\frac{q}{p}\frac{dB_y}{dx}x \quad +\frac{1}{2!}\frac{q}{p}\frac{d^2B_y}{dx^2}x^2 \quad +\frac{1}{3!}\frac{q}{p}\frac{d^3B_y}{dx^3}x^3 \quad +\dots \\ &= \frac{1}{R} \quad +k_1x \quad +\frac{1}{2!}k_2x^2 \quad +\frac{1}{3!}k_3x^3 \quad +\dots \end{aligned} \tag{3.4}$$

Here the multipole strength has already been normalized to the particle momentum to get an energy independent description of the magnetic components. The first term (1/R) of Equation (3.4) represents a dipolar field, the second term (k_1x) stems from a field generated by a quadrupole and the following terms represent fields from higher order magnets like sextupoles. Each one of these magnet types serves a specific purpose in a synchrotron. Dipoles are used to bend and steer the particle beam on the design trajectory. Quadrupoles focus or defocus the beam and ensure a stable, non-diverging beam. These two types make up the majority of the magnets in an accelerator and since their effect only depends linearly on the displacement these define linear dynamics. Higher order magnets like sextupoles are used to correct for examples chromaticity. A sequence of magnetic elements is commonly called magnetic lattice and a lattice only containing linear elements is correspondingly called linear lattice.
For a linear lattice and assuming small deviations from the reference orbit, one can derive the equation of motion for a particle with ideal momentum (see for example [17] for complete derivation)

$$u'' - K(s)u = 0 \tag{3.5}$$

where u represents either the x or y coordinate. $K(s)$ represents the focusing effect of dipoles and quadrupoles

$$K_x(s) = \left(\frac{1}{\rho(s)^2} - k_1(s)\right) \tag{3.6}$$

$$K_y(s) = k_1(s) \tag{3.7}$$

The term $1/\rho(s)^2$ stems from the weak focusing effect of the dipoles and it is only present in the bending plane. The term $k_1(s)$ arises from the strong (de-)focusing effect of the quadrupoles. When the radius of particle accelerator is large, the contribution of the weak focusing term can be neglected.
A general solution for this equation is

$$\begin{pmatrix} u(s) \\ u'(s) \end{pmatrix} = \begin{pmatrix} C(s) & S(s) \\ C'(s) & S'(s) \end{pmatrix} \begin{pmatrix} u_0 \\ u'_0 \end{pmatrix} \tag{3.8}$$

where u_0, u'_0 are the initial conditions. The matrix elements in the solution then depend on the component through which the particle is tracked.

In the following, the matrices for most important components will be presented

$$\text{Focusing Quadrupole} : \begin{pmatrix} \cos(\sqrt{k_1}s) & \frac{1}{\sqrt{k_1}}\sin(\sqrt{k_1}s) \\ -\sqrt{k_1}\sin(\sqrt{k_1}s) & \cos(\sqrt{k_1}s) \end{pmatrix} \tag{3.9}$$

$$\text{Defocusing Quadrupole} : \begin{pmatrix} \cosh(\sqrt{k_1}s) & \frac{1}{\sqrt{k_1}}\sinh(\sqrt{k_1}s) \\ \sqrt{k_1}\sinh(\sqrt{k_1}s) & \cosh(\sqrt{k_1}s) \end{pmatrix} \tag{3.10}$$

$$\text{Dipole} : \begin{pmatrix} \cos(\frac{s}{\rho}) & \rho\sin(\frac{s}{\rho}) \\ -\frac{1}{\rho}\sin(\frac{s}{\rho}) & \cos(\frac{s}{\rho}) \end{pmatrix} \tag{3.11}$$

$$\text{Drift Space} : \begin{pmatrix} 1 & s \\ 0 & 1 \end{pmatrix}. \tag{3.12}$$

With the above-presented matrices, the motion of a particle can be tracked through a linear lattice. The transfer matrix of a series of n elements with the matrices $M_1, M_2, ..., M_{n-1}, M_n$ is just the matrix product of these transfer matrices,

$$M = M_n \cdot M_{n-1} \cdot \ldots \cdot M_2 \cdot M_1. \tag{3.13}$$

In certain cases, it can be useful to describe the quadrupoles as elements with zero length. In this so called thin lens approximation, the transfer matrix for the magnets becomes

$$\begin{pmatrix} 1 & 0 \\ KL & 1 \end{pmatrix}. \tag{3.14}$$

A thorough derivation of the thin lens approximation can, for example, be found in [17].

3.4 Beta Function

In the previous section, it was shown that position of a single particle can be tracked through a linear lattice consisting of an arbitrary number of elements. However since for example, an LHC bunch contains around $1.15 \cdot 10^{11}$ particles [6] this approach becomes rather impractical for describing the whole particle beam. Instead, a different representation is commonly used which uses the beam envelope and will be derived in the following. In a circular accelerator $K(s)$ is piecewise constant, periodic function and with a period of C

$$K(s) = K(s + C), \tag{3.15}$$

where C is the circumference of the accelerator ring. With this constraint Equation (3.5) also constitutes a Hill's equation which allows to solve it using Floquet's theorem. It is solved by following equations

$$u(s) = \sqrt{\epsilon}\sqrt{\beta(s)}\cos(\psi(s) + \phi) \tag{3.16}$$

$$u'(s) = -\frac{\sqrt{\epsilon}}{\beta(s)}\left[\alpha(s)\cos(\psi(s) + \phi) + \sin(\psi(s) + \phi)\right] \tag{3.17}$$

which describes the transverse oscillation of a particle around the reference orbit. This pseudo-harmonic oscillation is also called betatron oscillation. The betatron-function $\beta(s)$ is the position dependent oscillation amplitude and defines together with the emittance of a single particle ϵ the beam envelope $\sqrt{\epsilon\beta}$. Here α equals $-\frac{1}{2}\beta(s)'$ and the constant ϕ is dependent on the starting conditions. In this solution, the phase advance $\psi(s)$ relates to the betatron amplitude function $\beta(s)$ via

$$\psi(s) = \int_{s_0}^{s} \frac{d\tau}{\beta(\tau)} \tag{3.18}$$

It is noteworthy that the betatron amplitude of all particles β does not depend on the initial conditions and is a property of the linear lattice.

3.5 Emittance and Phase space

Combining equations (3.16) and (3.17) one obtains the following equation

$$\gamma(s)x(s)^2 + 2\alpha(s)x(s)x'(s) + \beta(s)x'(s)^2 = \epsilon \tag{3.19}$$

where $\gamma(s)$ is defined as $\gamma(s) = \dfrac{1 + \alpha^2(s)}{\beta(s)}$. Together with β and α these three functions

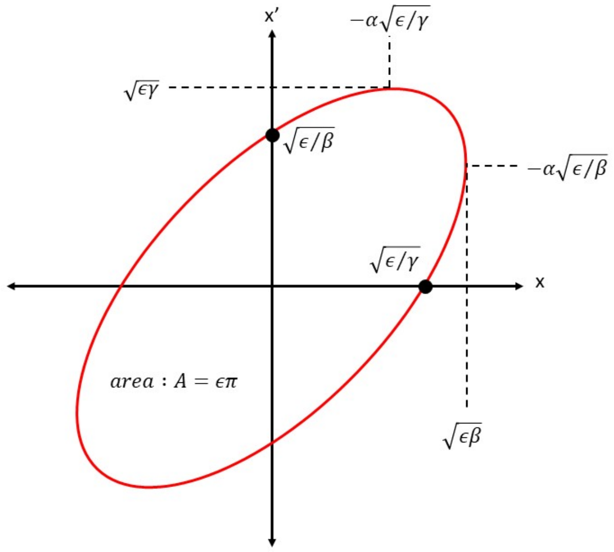

Figure 3.2: Phase space diagram.

are called Twiss parameters. The emittance ϵ calculated here is of one particle and hence is called single particle emittance. Its unit is m. The Equation (3.19) describes an ellipse in the phase space $(x(s), x'(s))$ with the area $\pi \cdot \epsilon$. The shape and orientation of the ellipse is determined by the Twiss parameters β, α, and γ as is illustrated in Figure 3.2. The Twiss parameters change as the beam is moving through the lattice so the phase space ellipse also gets transformed by focusing and defocusing elements. This transformation of the phase space ellipse after a focusing quadrupole is shown in Figure 3.3.

Given the Twiss parameters at an initial point β_0, α_0, and γ_0 the Twiss parameters in a given element can be obtained via

$$\begin{pmatrix} \beta(s) \\ \alpha(s) \\ \gamma(s) \end{pmatrix} = \begin{pmatrix} C^2 & -2CS & S^2 \\ -CC' & CS' + C'S & -SS' \\ C'^2 & -2C'S' & S'^2 \end{pmatrix} \cdot \begin{pmatrix} \beta_0 \\ \alpha_0 \\ \gamma_0 \end{pmatrix} \tag{3.20}$$

where

$$C = \cos\left(\sqrt{K}s\right), \quad S = \frac{1}{\sqrt{K}} \sin\left(\sqrt{K}s\right) \quad \text{in case of a focusing quadrupole,} \tag{3.21}$$

$$C = \cosh\left(\sqrt{K}s\right), \quad S = \frac{1}{\sqrt{K}} \sinh\left(\sqrt{K}s\right) \quad \text{in case of a defocusing quadrupole and} \tag{3.22}$$

$$C = 1, \quad S = s \quad \text{in case of a drift space.} \tag{3.23}$$

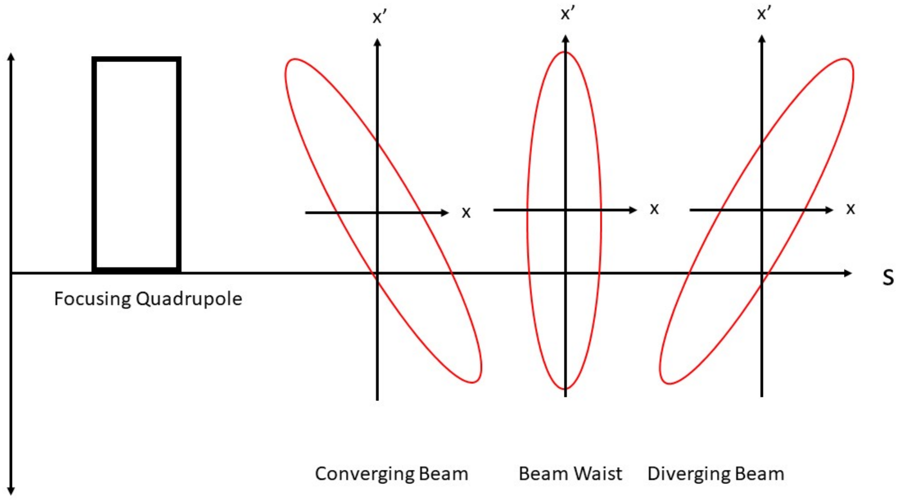

Figure 3.3: Evolution of the phase space ellipse in the drift space after a focusing quadrupole. Figure adapted from [17]

The transfer matrix for a series of accelerator elements is again the matrix product of the single transfer matrices.

In real colliders the beam consists of multiple particles, each one with a different single particle emittance $\epsilon_{single\ particle}$ and therefore differing oscillation amplitude. As the shape of ellipse is given by the Twiss parameters, the orientation of the ellipse is the same for all particles. The distribution of the single particle emittances is usually a Gaussian distribution. It is customary to describe the beam emittance ϵ as the RMS emittance of the particle beam.

$$\epsilon = \sqrt{\epsilon^2{}_{single\ particle}} \tag{3.24}$$

The actual beam size $\sigma(s)$ is then also given as 1σ of the Gaussian distribution.

$$\sigma(s) = \sqrt{\epsilon\beta(s)} \tag{3.25}$$

According to Liouville's theorem, the particle density in phase space remains constant over time if only conservative forces are exerted. If the accelerating electric fields of the RF-cavities are neglected this condition is generally met in particle accelerators. This means that as the beam is moving through the machine the beam emittance ϵ is conserved.

However, as particles are accelerated in the RF-cavities the emittance actually shrinks, a process which is called adiabatic damping. For this reason the normalized emittance

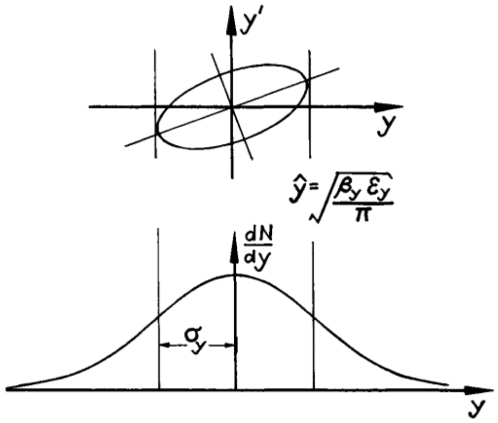

Figure 3.4: Schematic illustration of the emittance distribution [18]

$$\epsilon_N = \epsilon \beta_{rel} \gamma_{Lorentz} \tag{3.26}$$

with $\beta_{rel} = v/c$ and $\gamma_{Lorentz} = 1/\sqrt{1-\beta_{rel}^2}$, is introduced which remains constant during the acceleration process and allows comparison between phase space areas independent of the velocity.

3.6 Phase advance

As has been stated in a previous section, the phase advance between any two points in an accelerator can be calculated via Equation (3.18). Now for a circular collider, the phase advance over the whole ring divided by 2π gives the number of betatron oscillations per turn and it is called tune Q of the accelerator.

$$Q_{x,y} = \frac{1}{2\pi} \oint \frac{d\tau}{\beta_{x,y}(\tau)} \tag{3.27}$$

As the betatron motion in the transverse planes can be different, an accelerator lattice has a pair of tunes Q_x and Q_y called working point.
In a circular accelerator, particles pass through the same magnet every turn which can cause the excitation of resonant betatron oscillations due to magnetic imperfections. These resonances can occur if the following condition

$$m \cdot Q_{x,y} = p \quad (m, p \in \mathbb{Z}) \tag{3.28}$$

is met, with m being the order of the resonance. Such a resonant betatron oscillation is illustrated in Figure 3.5 where all but one magnet are assumed free of errors. The faulty magnet deflects the beam onto a bigger orbit each time the particle passes through until the oscillations amplitude becomes too big and the particle gets lost.

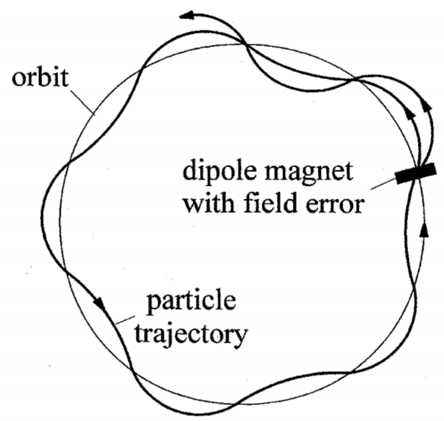

Figure 3.5: Resonant excitation of betatron oscillations by a dipole field error [19]

In the case of a coupling between the motion in the transverse planes the resonance condition becomes

$$mQ_x + nQ_y = p \quad (m, n, p \in \mathbb{Z}) \tag{3.29}$$

Since in modern accelerators higher order magnets like octupoles or dodecapoles are present, which can excite high order resonances, it is very important to choose a working point sufficiently far away from resonance lines when designing a storage ring. Possible feasible working points can be found using a tune diagram which is illustrated in Figure 3.6. Here the two axes represent the fractional parts of Q_x and Q_y and the resonance conditions are shown as lines.

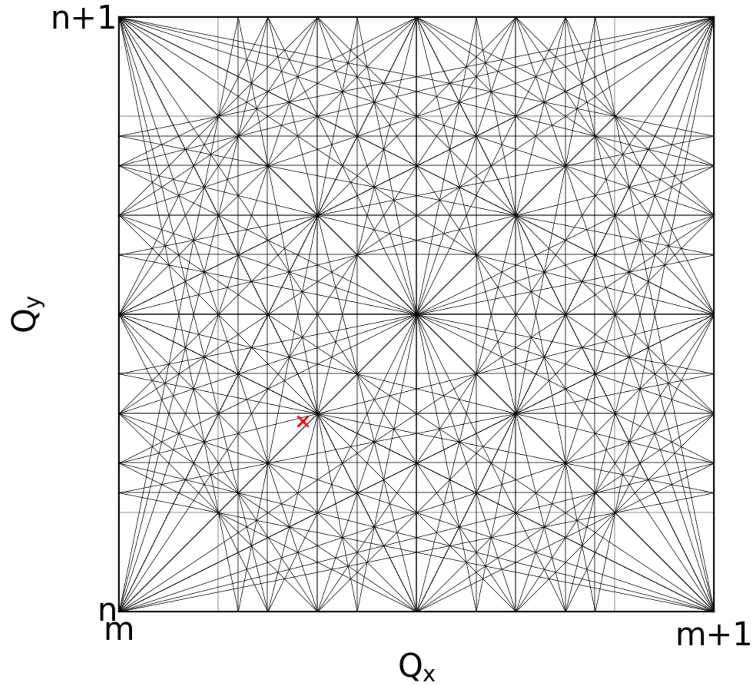

Figure 3.6: Resonance diagram up to 6th order. The nominal working point of the LHC and FCC-hh (.31,.32) during collision is marked with a red cross.

3.7 Dispersion and Chromaticity

Up until this section, only a particle traveling on the design orbit and with the design momentum p has been discussed. However, to describe the motion of an off-momentum particle Equation (3.5) has to be extended. In case of a non-zero $\Delta p/p$ Equation (3.5) becomes

$$x''(s) + \left(\frac{1}{\rho^2(s)} - k_1(s)\right) x(s) = \frac{1}{\rho(s)} \frac{\Delta p}{p}. \tag{3.30}$$

The general solution to Equation (3.30) consists of a linear combination of the solution of the homogeneous part x_h and a partial solution of the inhomogeneous equation x_{in}

$$x = x_h(s) + x_{in}(s). \tag{3.31}$$

Here $x_h(s)$ is the betatron oscillation amplitude of an ideal particle with a design momentum p and $x(s)_{in}$ describes an additional orbit displacement because of the momentum deviation. A special solution to the inhomogeneous equation is then

$$x_{in}(s) = D(s)\frac{\Delta p}{p}, \tag{3.32}$$

where $D(s)$ is the solution to

$$D''(s) + \frac{1}{\rho^2(s)}D(s) = \frac{1}{\rho(s)}. \tag{3.33}$$

and is called the dispersion function. At a given position s the dispersion D(s) is given by

$$D(s) = \frac{\sqrt{\beta(s)}}{2\sin(\pi Q)}\int_s^{s+C}\frac{\sqrt{\beta(\tau)}}{\rho(\tau)}\cos\left(\mu(\tau) - \mu(s) - \pi Q\right)d\tau. \tag{3.34}$$

The oscillation amplitude thus becomes

$$x(s) = \sqrt{\beta_x \epsilon} + D(s)\frac{\Delta p}{p}. \tag{3.35}$$

The orbit length of a particle with a non-zero $\Delta p/p$ also differs from the design orbit length due to this displacement. This can easily be seen from Equation (3.3) where for a constant magnetic field the bending radius ρ varies with the particle momentum. The difference in orbit lengths can in first-order be calculated using

$$\frac{\Delta C}{C} = \alpha_c \frac{\Delta p}{p} \tag{3.36}$$

where C is the circumference of the accelerator and α_c the momentum compaction factor, which is an energy independent quantity and determined by the lattice design. The change in accelerator circumference ΔC is given by

$$\Delta C = \frac{\Delta p}{p}\oint \frac{D(s)}{\rho(s)}ds, \tag{3.37}$$

and the momentum compaction factor α_c can be obtained via

$$\alpha_c = \frac{1}{C}\oint \frac{D(s)}{\rho(s)}ds. \tag{3.38}$$

The momentum deviation not only affects the trajectory of a particle moving in an accelerator but also focusing strength of a quadrupole. This momentum dependent quadrupole strength is given by

$$k_1(p) = -\frac{q}{p}\frac{dB_y}{dx} = -\frac{q}{p_0 + \Delta p}\frac{dB_y}{dx} \approx -\frac{q}{p_0}\left(1 - \frac{\Delta p}{p_0}\right)\frac{dB_y}{dx} = k_1 - \Delta k \tag{3.39}$$

where $\Delta k = \frac{\Delta p}{p} k_1$ is the quadrupole error due to the momentum offset. These quadrupole errors also induce a tune shift in the accelerator proportional to the momentum deviation.

$$\Delta Q = \frac{1}{4\pi} \int \beta(s) \Delta k_1(s) ds \approx -\frac{1}{4\pi} \frac{\Delta p}{p} \int \beta(s) k_1(s) ds \tag{3.40}$$

The natural chromaticity of an accelerator is then defined as

$$Q'_{x,y} = \mp \frac{\Delta Q_{x,y}}{\Delta p/p} = \frac{1}{4\pi} \int \beta_{x,y}(s) k_1(s) ds \tag{3.41}$$

From Equation (3.41) it can be seen that the biggest contribution to the chromaticity usually comes from the triplet quadrupoles in the experimental insertions as the β-functions reaches its maximum there. Due to the often considerable tune shifts even for small momentum deviations, the chromaticity has to be corrected in order to avoid crossing optical resonances and thereby losing particles. To compensate for the momentum dependent quadrupole strength and decrease chromaticity and thereby the tune shift, correction should take place where particle are sorted according to their momentum i.e. in a region with a high dispersion. Here sextupole magnets are placed as they feature a transverse beam position dependent focusing strength. The sextupole field is given by

$$B_x = \frac{d\psi}{dy} = \frac{1}{2} m(x^2 - y^2) \tag{3.42}$$

$$B_y = \frac{d\psi}{dx} = mxy. \tag{3.43}$$

The equations of motion in the presence of sextupoles are then

$$x'' + k_1 x = k_1 x \frac{\Delta p}{p} - \frac{1}{2} m(x^2 - y^2), \tag{3.44}$$

$$y'' - k_1 y = -k_1 y \frac{\Delta p}{p} + mxy. \tag{3.45}$$

Here, the weak focusing term $\frac{1}{\rho^2(s)}$ has been omitted. Assuming no dispersion in the y-axes, x and y can be written as

$$x = x_h + D(s) \frac{\Delta p}{p}, \qquad y = y_h \tag{3.46}$$

where x_h describes the betatron oscillation of an on-momentum particle. Using Equation (3.46) to expand Equations (3.44) and (3.45) and neglecting second or higher order terms one obtains

$$x_h'' + k_1 x_h = (k_1 - mD(s))\, x_h \frac{\Delta p}{p} \tag{3.47}$$

$$y_h'' - k_1 y_h = -(k_1 - mD(s))\, y_h \frac{\Delta p}{p}. \tag{3.48}$$

The pertubations on the right-hand side have the character of a gradient error and thus lead to a tune shift. Using these, the chromaticity becomes

$$Q'_{x,y} = \mp \frac{1}{4\pi} \int \beta_{x,y}(s)\, [k_1(s) + m\, D(s)]\, ds. \tag{3.49}$$

Usually, the sextupoles are placed next to the quadrupoles in the accelerator arc as there the dispersion is highest, thus reducing the required sextupole strength and the β-functions of the transverse planes are well separated minimizing the effect on the other plane.

3.8 Coupling

Up to this point, the motion in the two transverse planes has been treated independently from another. This way the trajectory can be described as

$$\begin{pmatrix} x(s) \\ x'(s) \\ y(s) \\ y'(s) \end{pmatrix} = \begin{pmatrix} C_x(s) & S_x(s) & 0 & 0 \\ C_x'(s) & S_x'(s) & 0 & 0 \\ 0 & 0 & C_y(s) & S_y(s) \\ 0 & 0 & C_y'(s) & S_y'(s) \end{pmatrix} \begin{pmatrix} x_0 \\ x_0' \\ y_0 \\ y_0' \end{pmatrix} = \begin{pmatrix} M_1(s) & 0 \\ 0 & M_2(s) \end{pmatrix} \begin{pmatrix} x_0 \\ x_0' \\ y_0 \\ y_0' \end{pmatrix} \tag{3.50}$$

where C_x, S_x, C_y, S_y and their respective derivatives are the matrix elements from Equations (3.9), (3.10), (3.11) and (3.12) for a given magnetic element. However due misalignments of quadrupoles, orbit errors in higher order magnets like sextupoles or the use of a solenoid in an experiment as for example it is the case in CMS [20] a coupling between the horizontal and vertical motion is introduced. When including coupling stemming from skew quadrupoles and solenoidal fields the equations of motion become

$$x'' + k(s)x = -k_{skew}(s)y + S(s)y' + \frac{1}{2}S'(s)y \tag{3.51}$$

$$y'' - k(s)y = -k_{skew}(s)x + S(s)x' + \frac{1}{2}S'(s)x, \tag{3.52}$$

where K_{skew} is the normalized skew quadrupole strength and S the normalized solenoidal field strength. In this case Equation (3.50) is rewritten as

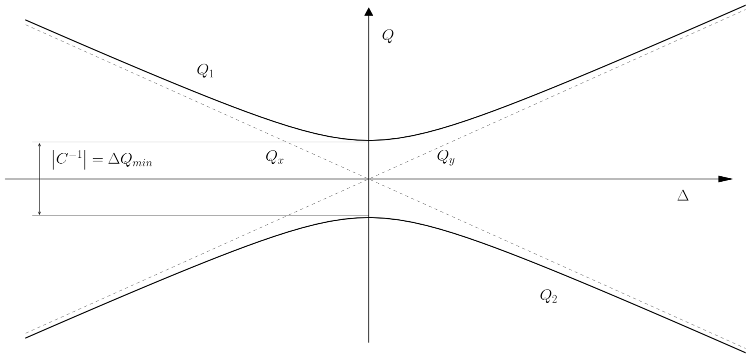

Figure 3.7: Illustration of the effect of coupling on the tunes.

$$\begin{pmatrix} x(s) \\ x'(s) \\ y(s) \\ y'(s) \end{pmatrix} = \begin{pmatrix} M_1(s) & N_1 \\ N_2 & M_2(s) \end{pmatrix} \begin{pmatrix} x_0 \\ x'_0 \\ y_0 \\ y'_0 \end{pmatrix}. \tag{3.53}$$

As discussed in an earlier section in the presence of coupling if m and n in Equation (3.29) are integer values coupling resonances can occur. Furthermore the tunes Q_x and Q_y are not the eigentunes anymore instead

$$Q_1 = Q_x - \frac{\Delta}{2} + \frac{1}{2}\sqrt{\Delta^2 + (C^-)^2} \tag{3.54}$$

$$Q_2 = Q_y - \frac{\Delta}{2} - \frac{1}{2}\sqrt{\Delta^2 + (C^-)^2} \tag{3.55}$$

becoming the new eigentunes. Here Δ represents the uncoupled fractional tune split ($\Delta = |Q_x - Q_y| - p$, p being the integer tune split) and C^- coupling coefficient. From Equations (3.54) and (3.55) one can see that the fractional part of these new eigentunes can never be equal and the closest tune difference is C^-. This is illustrated in Figure 3.7.

3.9 Beam-Beam effects

During every bunch crossing in the collision regions of a particle accelerator, only a few particles of a given bunch collide with particles from the counter-rotating beam. Yet most of the particles experience a kick due to the Lorentz force coming from the electromagnetic field generated by the opposite beam which in the case of beams with the same charge is repellent. The radial kick $\Delta r'$ coming from the opposite beam experienced by a particle is

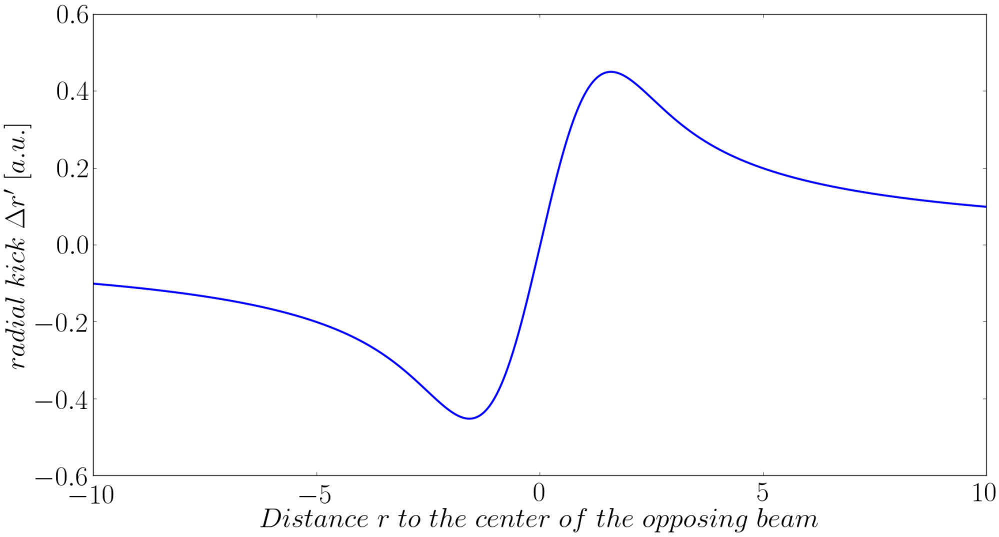

Figure 3.8: Radial Kick due to head-on beam-beam interaction. Kick amplitude is given in arbitrary units and the distance is given in units of r.m.s. beam size.

$$\Delta r' = -\frac{2Nr_0}{\gamma}\frac{1}{r}\left[1 - \exp\left(-\frac{r^2}{2\sigma^2}\right)\right] \tag{3.56}$$

where N is the total number of particles, r_0 the classical particle radius, $r_0 = \frac{1}{4\pi\epsilon_0}\frac{e^2}{m_0c^2}$, r the distance to the opposing beam center and σ the beam size. Note also that here round beams ($\sigma = \sigma_x = \sigma_y$) and a Gaussian beam density distribution are assumed.

In Figure 3.8 the general shape of kick amplitude as a function of r is presented and from this, it can be seen that for small amplitudes r the kick is linear. At this small amplitudes, the linear field experienced by the beam acts like a quadrupole and induces a tune shift ΔQ_{ho}. For a working point far enough away from linear resonances this tune shift is roughly equal to the linear beam-beam parameter ξ

$$\xi = \frac{Nr_0\beta^*}{4\pi\gamma\sigma^2} \tag{3.57}$$

a parameter which is often used to quantify the strength of the beam-beam interaction. To avoid large tune shifts the number of particles per bunch is actually limited by this beam-beam parameter which then in turn also limits the attainable peak luminosity. In order to avoid these beam-beam interactions during phases like filling the storage ring or ramping the energy, the two beams are separated. Once the beams are set up for collision mode they are steered to collide only in the Interaction point under a crossing angle. This way secondary head-on collisions in the common vacuum pipe region, which would possibly lead to strong beam perturbations, can be avoided. The bunches of one beam exert electromagnetic forces on the opposing beam. This so-called long-range interaction, schematically illustrated in Figure 3.9, also induces a tune shift which depends on the separation between the beams.

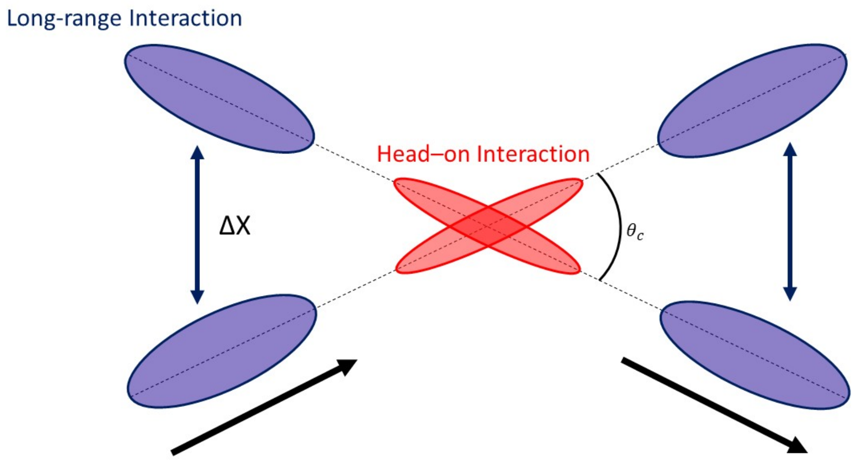

Figure 3.9: Beam-beam interactions in particle collider interaction point.

For a large enough separation the long-range tune shift ΔQ_{lr} roughly follows

$$\Delta Q_{lr} \propto -\frac{N}{\Delta X^2} \tag{3.58}$$

with N being the bunch intensity and ΔX the separation in sigma.

The tune shift caused by long-range interaction has opposite sign in the separation plane compared to the head-on tune shift. This property can be used to partially compensate the beam-beam tune shift by having different separation planes in the interaction regions.

3.10 Optics Matching and Beam optics codes

When designing an accelerator lattice usually smaller subparts like the arc cells and the insertion regions are designed first and combined afterwards. At the transition point between two such building blocks, the optical parameter need to be matched

$$(\beta_x, \beta_y, \alpha_x, \alpha_y, D_x, D'_x)_l = (\beta_x, \beta_y, \alpha_x, \alpha_y, D_x, D'_x)_r \tag{3.59}$$

to allow for periodic solution in a circular accelerator or to avoid dilution of particles in phase space if a beam is transfered from a beam transfer line to an accelerator. Furthermore also the optical functions in the insertion need to be controlled as for example excessive β-functions need to be avoided to not exceed the aperture of the vacuum chamber. To allow for an optimal condition for the experiments the optical functions at the Interaction point (IP) should also be matched to certain values. Usually, the α-function should be 0 in the IP to ensure that beam waist is at the designed interaction point.Furthermore the dispersion function is also matched to 0 to avoid an increased beam size due to momentum deviation as can be seen from Equation (3.35). Depending on which setting the accelerator is run and the experimental goal the matched β-function in the IP (β^*) can be either matched to the lowest possible values to achieve peak instantaneous luminosity or in case of Van der Meer scans or elastic scattering and diffractive physics event studies to a rather high $\beta *$ which is preferred in these scenarios [21, 22]. The matching of the optical functions is done by adjusting the strength k_1 of all the quadrupoles in a given insertion. During the matching additional constraints in the section may be required to impose to avoid for example excessive β-functions or allow for specific phase advances. Since even for simple insertions the vast number of variables makes solving these problems analytically impossible, numerical optimization routines are used. Such numerical optimization routines are integrated in various accelerator physics code packages such as SAD [23] or MAD-X [24]. However, the existence of a solution fitting all the imposed constraints is not guaranteed. Even if a matching solution is found, there is no guarantee that the found option is the best solution as these algorithms might be stuck in a local minimum. It is therefore important to start with a good initial guess to converge to the optimal solution.

In the context of this thesis, MAD-X (Methodical Accelerator Design) has been used which is an open-source, general purpose accelerator code package developed and maintained by CERN. MAD-X supports a wide range of elements for designing accelerator lattices like Beam Position Monitors, Crab Cavities, Electrostatic separators and RF-cavities with each requiring some common properties like length, position, and aperture but also more specific properties like for example Voltage, Phase lag, and frequency for the case of a RF-cavity [25].

MAD-X's MATCH module also allows matching various local ($\beta, \alpha, D_x, \ldots$) as well as global properties (Q, Q') using different matching algorithms like the fast gradient minimization or simplex algorithm.

Given the elements apertures, tolerances and beam parameters like emittance the APERTURE module in MAD-X allows calculating how much of the available aperture is occupied by the beam.

Also included is the possibility to conduct single particle tracking studies using either MAD-X's own tracking algorithm or the Polymorphic Tracking Code (PTC) [26].

With MAD-X it is also possible to generate input files for the tracking code Sixtrack [27]. Sixtrack is a 6D symplectic single particle tracking code developed and maintained by CERN and it is used to conduct dynamic aperture studies (see Chapter 6), collimation studies and beam-beam studies for LHC, HL-LHC and FCC. It was specifically designed to work with large circular colliders and with special tools it allows to run a large number of tracking jobs using the LHC@Home computing grid [28] or the CERN Computing Grid. In this thesis, Sixtrack has been used to study the effect of magnetic errors on the Dynamic Aperture.

CHAPTER 4

Interaction Region Design

The adaptation of the strong focusing or alternating-gradient focusing principle, first proposed by N. Christofilos [29] and later on independently developed and published by E. Courant, M. Livingston, H. Snyder and J. Blewett [30], signified a great step forward towards the large scale particle colliders which are currently in operation. The transition from the weak focusing principle allowed to separate synchrotrons in smaller components each having a specific function. The lattice can now be split into two general supersections, the rounded arc section and the straight sections housing insertion with a specific function, giving the lattice a more round-cornered shape. Whereas the arc section is used for bending the beam while keeping the beam size at a reasonable level, the straight sections host for example particle detectors, RF-cavities for accelerating the beams and collimators to remove specific particles with either a too large momentum deviation or transverse amplitude.

This section starts with one of the key figures for any particle collider, the luminosity. Afterwards, the units out of which experimental and injection insertion are made of are discussed in detail. The section is closed with constraints coming from hardware which needs to be taken into consideration when designing the insertions.

4.1 Luminosity

One of the key figures of merit for any particle collider is the luminosity $\mathscr{L}$ typically measured in $\mathrm{cm}^{-2}\mathrm{s}^{-1}$. It is determined by the accelerator lattice and the beam parameters and relates to the number of events via

$$\frac{dR}{dt} = \mathscr{L}\sigma \tag{4.1}$$

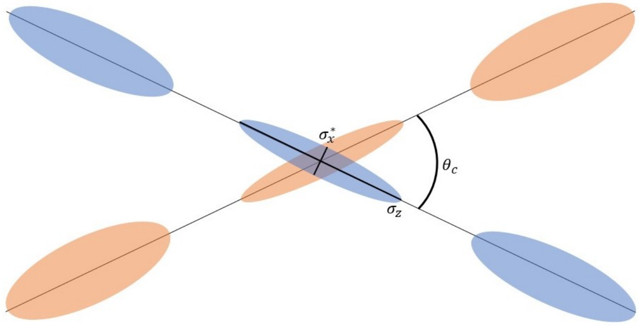

Figure 4.1: Simplified bunch collision scheme with a crossing angle θ_c and the longitudinal and transversal bunch dimensions σ_z and σ_x

where σ is the cross section of the event and R the number of events. Assuming Gaussian beams of equal size the instantaneous luminosity can be calculated using [31]

$$\mathscr{L} = \frac{N_1 N_2 f n_b}{4\pi\sigma_x^*\sigma_y^*} S(\phi, \sigma_x, \sigma_z). \tag{4.2}$$

Here $N_{1,2}$ are the number of particles in bunch 1 and 2 respectively, n_b the number of colliding bunches, f the beam revolution frequency, σ_x^* and σ_y^* the transverse beam size at the interaction point. The transverse beam size is calculated via $\sigma_{x,y}^* = \sqrt{\epsilon\beta_{x,y}^*}$ where ϵ is the emittance of the beam and β^* the β-function in the interaction point. As the beam parameters like n_b and ϵ are usually determined by other factors the most important parameter in terms of optics design is β^*. S is the geometric loss factor which results from the bunches colliding under a non-zero crossing which is illustrated in Figure 4.1.

The geometric loss factor S when assuming $\beta^* \gg \sigma_z$ is given by [31]

$$S = \frac{1}{\sqrt{1 + \left(\frac{\phi\sigma_z}{2\sigma_x^*}\right)^2}}, \tag{4.3}$$

where ϕ is the crossing angle, σ_z the longitudinal beam size and σ_x^* the transverse beam size in the crossing plane.

Another closely related key figure is the integrated luminosity since this gives a measure of how many collisions can be acquired by the experiments. It is calculated as follows

$$L = \int_0^T \mathscr{L}(\tau) d\tau, \tag{4.4}$$

where T is the total time in collision mode. The integrated luminosity is usually given in b^{-1}. Due to beam decay processes like rest gas collisions, intra beam scattering but also collisions with the opposing beam the instantaneous luminosity is not constant during a fill but decreases over time. When the luminosity drops below a certain level the beams are dumped and a new fill starts.

4.2 Experimental insertion

In colliders like LHC or FCC-hh, the beams move in separated beam pipes in opposite direction as illustrated in Figure 4.2 for the LHC.

Only in the experimental insertions the beams share the same beampipe. They are separated using orbit correctors to avoid unwanted collisions and brought into collision at the interaction point. The experimental insertions can be subdivided into different sectors, which is illustrated in Figure 4.3. The innermost part of the insertion is the interaction point (IP) where the particle collisions take place. The final focus system (FFS) is a special magnet structure used to focus both beams and achieve a minimum beam size at the IP. In the FFS both beams share the same beam pipe. In the separation section (SEP) two dipoles are used to separate the beams into different beam pipes. Downstream of the separation section is the matching section (MS) containing quadrupoles, which are used to match the optics functions to the periodic solution of the arc. In between the MS and the arc lies the dispersion suppressor (DIS). It aims to reduce the dispersion function in the insertion to zero. A more detailed description of the different sectors is given in the following sections.

The magnets in the insertion are usually labeled by their type and their position respective to the IP. For example, as the first quadrupole of the triplet is the innermost quadrupole, its label is Q1. The separation dipole, being the first dipole downstream of the triplet, is labeled as D1.

4.2.1 Final Focus System

A quadrupole does only allow to focus the beam in one plane while it defocuses the beam in the other transverse plane. Still, as can be seen from Equation (4.2) one wants to achieve small β-functions in both the x- and y- planes in order to maximize the instantaneous luminosity. This can be achieved by special final focusing structures like doublets, consisting of two quadrupoles and triplets, consisting of three quadrupoles. While doublets are usually only used in electron-positron colliders to generated flat beams ($\beta_x^* \gg \beta_y^*$) triplet structures are most commonly used in hadron colliders. Triplets provide the flexibility to generate round beams ($\beta_x^* = \beta_y^*$) as well as flat beams.

As the drift space between IP and the first quadrupole should be rather large to accommodate the particle detectors and the β-function grows with

$$\beta(s) = \beta^* + \frac{s^2}{\beta^*} \tag{4.5}$$

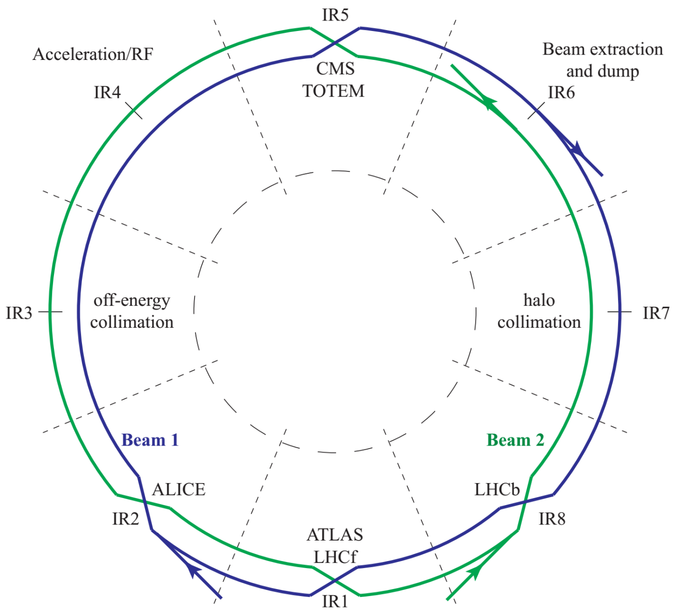

Figure 4.2: Schematic layout of the LHC with the four experimental insertions located in IR1, IR2, IR5 and IR8 [32]

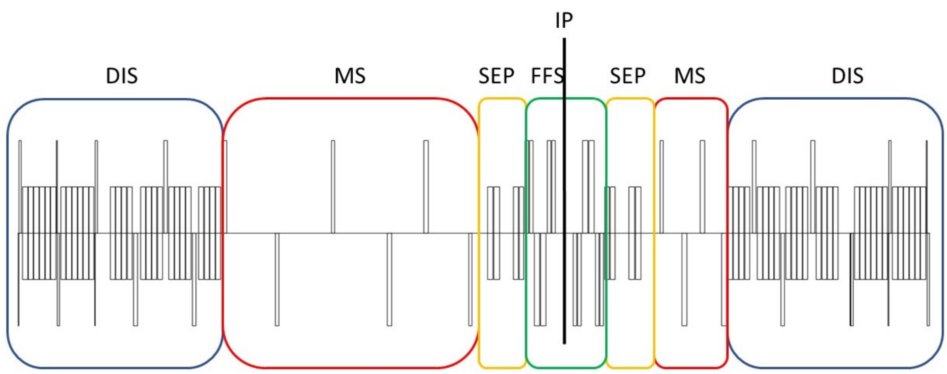

Figure 4.3: Insertion layout of a experimental insertion

the aperture of these final focus quadrupole needs to be large to allow for the large β-functions in the triplet created by a small β^*. The aperture of the quadrupole is not a free parameter but is limited by the required gradient and the feasible peak field in the coil via

$$R = B_{peak}/G \tag{4.6}$$

where R is the inner coil radius, B_{peak} the peak magnetic field and G the required gradient in Tm^{-1}. The peak field itself depends amongst others on the used superconductor, temperature and current. Due to the high β-functions in the triplet, the beam in this region is also very sensitive to field imperfections of the quadrupoles. For example in the LHC, the Dynamic aperture during collision is mainly determined by the field imperfections of the triplet quadrupoles and the separation and recombination dipoles [33].

As the final focusing quadrupoles are the closest to interaction point they are hit by some of the debris coming from the particle collision. The energy deposited in the superconducting magnets by these debris particles can be sufficient to quench the magnets. In order to avoid this scenario shielding material is put in front of the first quadrupole as well as inside the magnet aperture. This shielding in the quadrupoles reduces the available free aperture for the beam thus limiting the maximum β-function in the final focusing structure and the achievable minimum β^*, therefore a trade off needs to be found.

Orbit Correctors for Crossing Angle

In the final focusing system the counter rotating beams share the same beam pipe. To ensure that collisions only occur at the interaction point dipole corrector magnets are installed in the triplet and after the separation section. The combined corrector magnets allow to steer the beam in both horizontal and vertical planes to ensure a sufficient separation of the beams in the triplet. Furthermore, they can be used to correct for field imperfections and misalignments. An interaction region, showing the triplet quadrupoles and orbit correctors, is illustrated in Figure 4.4.

4.2.2 Separation Section

The separation section, located next to final focus system is used to separate the two counter rotating beams into separate beam pipes. It consists of two dipoles D1 and D2 which feature a special design. D1 , illustrated in Figure 4.5a, is a single bore dipole closer to final focus system. D2, as shown in Figure 4.5b, is a 2-in-1 dipole. In the case of the LHC and the FCC-hh where beam 1 and beam 2 have the same charge but opposite directions the bending fields need to point in the same direction.

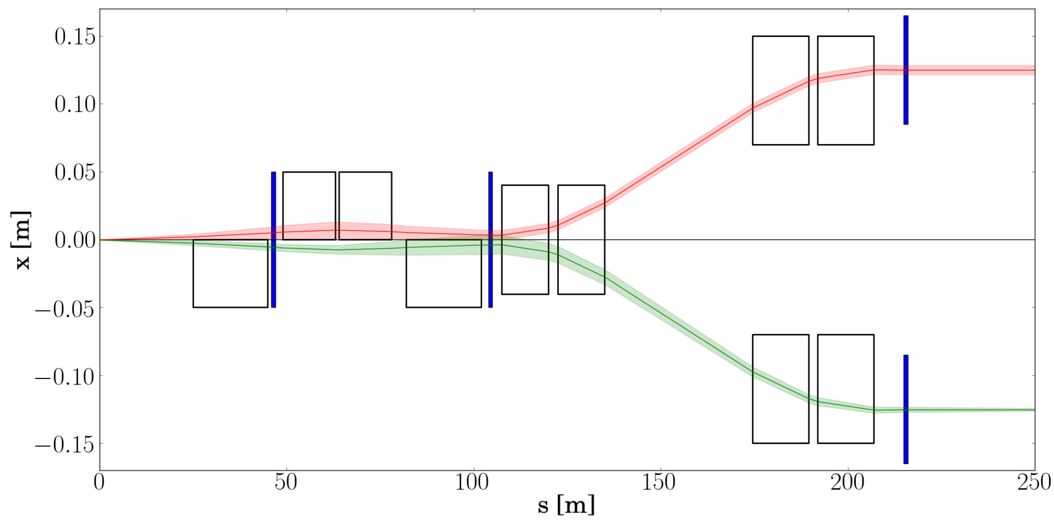

Figure 4.4: Illustration of an Interaction region with the triplet quadrupoles, separation and recombination dipoles and the orbit correctors in blue.

As the electromagnetic crosstalk between the coils should be mitigated as best possible, the aperture of the coils and the achievable field are both limited. These dipoles also create dispersion which has to be compensated to avoid having dispersion at the IP.

4.2.3 Matching Section

The matching section, located between the separation section and the dispersion suppressor, is composed of individually powered 2-in-1 quadrupoles which are used to match the optics function $\beta_x, \beta_y, \alpha_x, \alpha_y, D_x$ and D'_x to the arc. As with the triplet quadrupoles, it can be required to use individual aperture quadrupole magnets in this section. However as the debris coming from the IP is at this point significantly reduced, absorber material in the aperture of the magnet is often not needed.

4.2.4 Dispersion Suppressor and Arc

In order to ensure a minimum beam size for a maximum instantaneous luminosity the dispersion function $D(s)$ has to vanish at the interaction point. Therefore the dispersion coming from the dipoles in the arc needs to be suppressed which is done by means of a dispersion suppressor located on both sides of the insertion. In addition, the dispersion suppressor helps in matching the optics to the periodic arc solution. There exists various dispersion suppressor schemes: full-bend schemes, half-bend scheme, missing bend schemes and various combinations of these schemes. A more detailed description of dispersion suppressor schemes and derivation of the required relations of field strength and distances between the magnets can be found in [35].

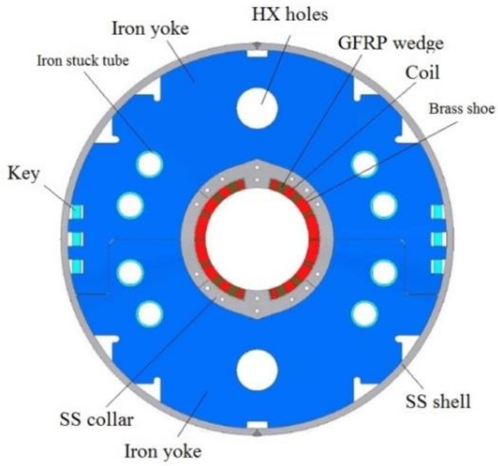

(a) Schematic of the D1 Dipole

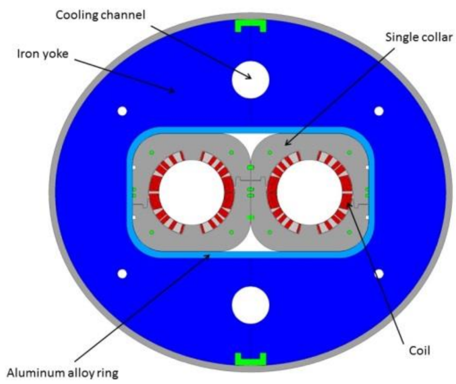

(b) Schematic of the D2 Dipole

Figure 4.5: Schematics of the dipoles in the separation section [34]

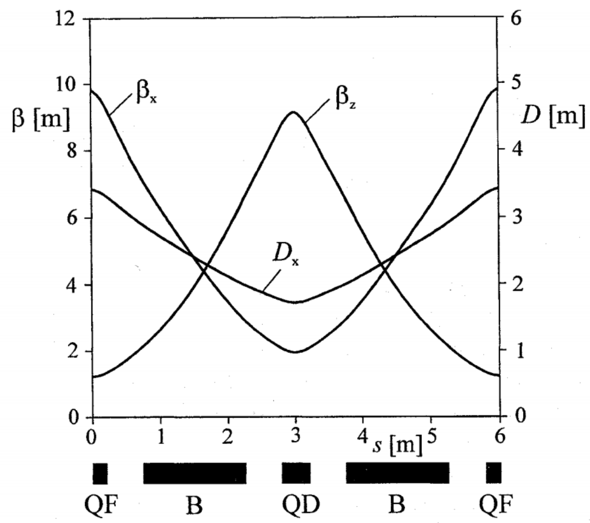

Figure 4.6: Schematic of a FODO cell together with the beam optic functions [19]

The arc section consists of a repeated sequence of lattice units, also called arc cells. An arc cell is a magnetic structure matched so that the twiss parameter $\beta_{x,y}$, $\alpha_{x,y}$ and $\gamma_{x,y}$ as well as the horizontal dispersion and its derivative D_x, D'_x are equal at the beginning and at the end of the structure. This allows to easily chain them together resulting in an arc section. The arc cells also contain the bending dipoles as well as other magnets like smaller quadrupoles for tune control and sextupoles for chromaticity compensation. A wide variety of magnetic lattices exists for the use as arc cells. Here only the most common and simplest type, the FODO cell, is explained in further detail. A more detailed discussion of other arc cell types commonly used in synchrotrons like the double - and triplet bend achromat lattice (DBA and TBA) or the triplet achromat lattice (TAL) can be found for example in [17].

The FODO structure consists of a focusing quadrupole (F) followed by a defocusing quadrupole (D) separated and terminated by a drift space (indicated by 0), illustrated in Figure 4.6. The arrangement is therefore F-0-D-0 hence this lattice structure is commonly called FODO cell. Usually, the drift space is occupied by a bend dipoles (B) which, if weak focusing is ignored, does have no impact on the β-functions.

The maximum and minimum β-function, occurring in the focusing and defocusing quadrupole respectively, in a plane is determined by length of the FODO-cell and the phase advance ϕ via

$$\hat{\beta} = \frac{L\left(1 + \sin(\frac{\phi}{2})\right)}{\sin(\phi)}, \qquad \check{\beta} = \frac{L\left(1 - \sin(\frac{\phi}{2})\right)}{\sin(\phi)}. \tag{4.7}$$

Figure 4.7 illustrates both $\hat{\beta}$ and $\check{\beta}$ as a function of phase advance for a given cell length of 100 m.

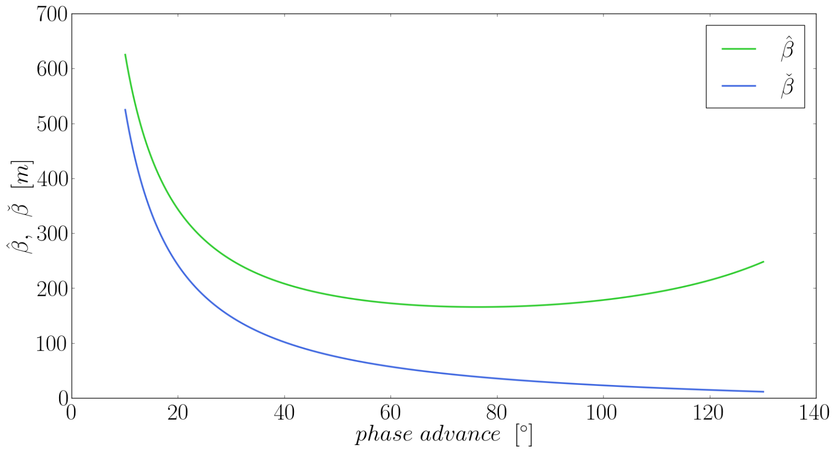

Figure 4.7: Maximum and minimum β-function in a FODO -cell

From this Figure, it can easily be seen that as the phase advance increases $\check{\beta}$ decreases. However, the maximum β-function $\hat{\beta}$ reaches its minimum at around 76°. For proton beam with $\epsilon_x \approx \epsilon_y$ one can derive that the best phase advance in terms of aperture requirement is $\phi = 90°$ [35].

4.3 Injection Insertion

The injection insertion is another critical component of any particle accelerator. It should allow to transfer the beams coming from either a linear or a circular preaccelerator safely to another machine with minimum beam loss and dilute the beam emittance as little as possible to provide not only the best possible beam quality for the experiments but also ensure machine safety.

In a conventional single turn injection scheme, illustrated in Figure 4.8, the incoming beam from a transfer-line passes a septum (MSI) which steers the beam into the accelerator aperture.

A septum is a special boundary separating two adjacent beams where only one of the beams is manipulated while the other beam is unaffected. The manipulation can be performed by either an electrostatic field, magnetostatic field or an electrodynamic field. As the use of electric fields to deflect high energy particle beams is unfeasible only magnetic septa are used in high energy colliders. The required abrupt magnetic field change between the two beam pipes can be achieved with various designs [37]. One such design, the Lambertson septum, is illustrated in Figure 4.9. This septum features very low leakage fields but the beam deflection is perpendicular to the beam displacement axis.

After the septum, the beam is then deflected onto the closed orbit of the accelerator by kicker magnet (MKI). A kicker magnet is a pulsed dipole magnet with a very fast rise and fall time in the order of 100 nanoseconds and a pulse width of up to

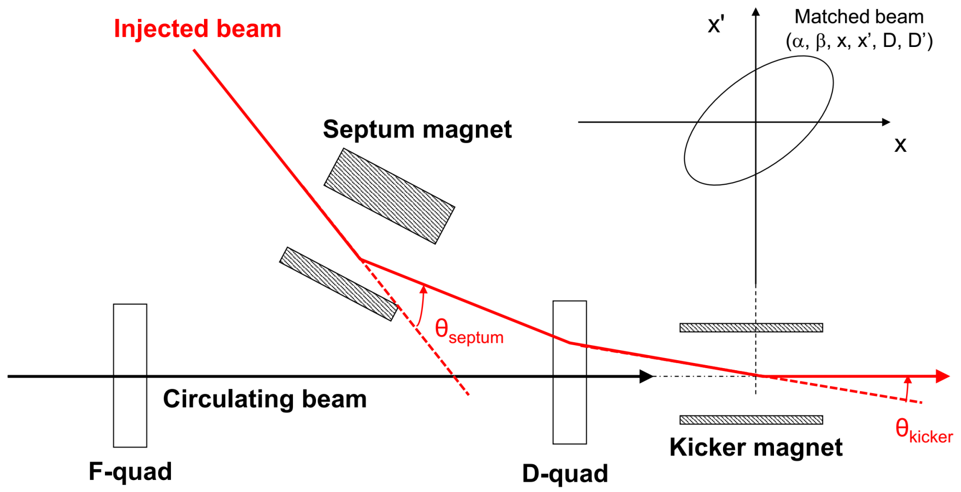

Figure 4.8: Schematic layout of a single turn injection insertion [36]

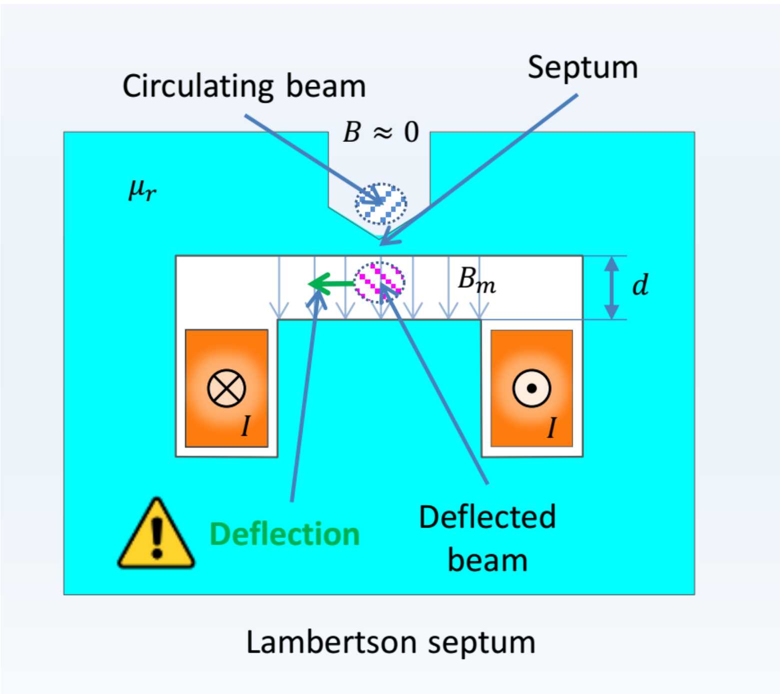

Figure 4.9: Cross section of a lambertson type septum [37]

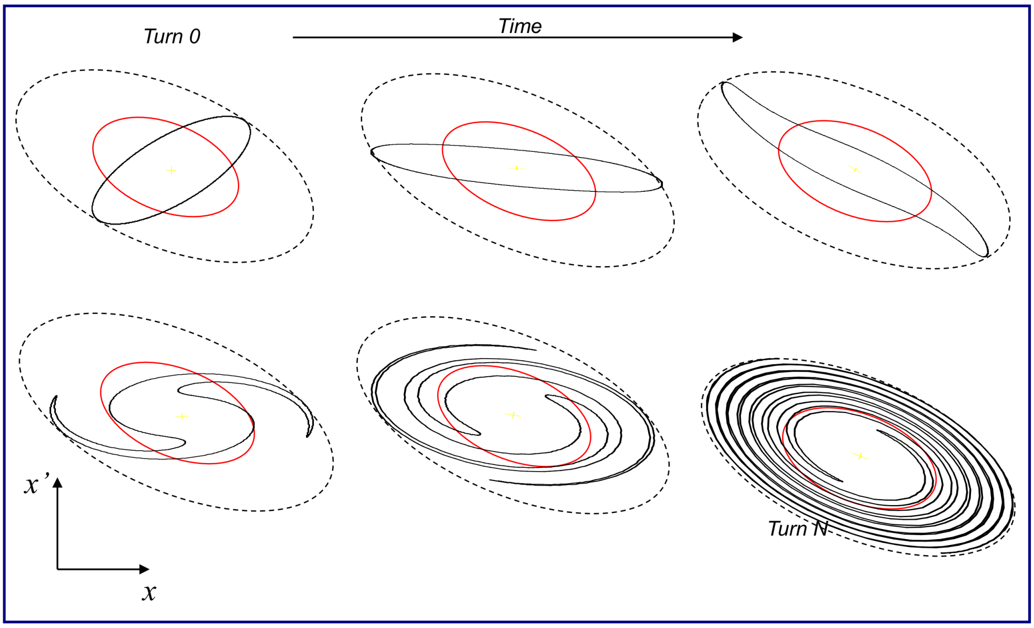

Figure 4.10: Filamentation of an injected beam due to optics mismatch [36]

microseconds [38]. By using such short pulses the injected bunch can be steered onto the closed orbit while already circulating bunches coming before or after the injected bunch are not affected. A quadrupole which is defocusing in the injection plane can be placed between the septum and the kickers to provide an extra kick and decrease the required kicker strength. To protect the accelerator machine equipment against failures from the injection kicker system like a mistimed turn-on or no turn-on at all, a dedicated injection protection absorber (TDI) is installed downstream of the kickers. The TDI is a movable absorber which has to withstand the impact of an injected bunch train. Its robustness is, therefore, one of the main limiting factors when trying to reduce the fill time of an accelerator as it determines the number of transferable bunches.

When designing the beam optics for such an injection insertion a certain number of constraints need to be respected to safely inject the beam with minimum beam dilution. The first requirement is that the injected beam optics parameters β_x, β_y, α_x, α_y, D_x, and D'_x at the entry point of the ring are matched to the optics of the ring. A mismatch of these would result in filamentation and an increased emittance as is illustrated in Figure 4.10.

If an injected beam is not placed on a central orbit due to for example a kick error or steering error in the transfer line, the beam will oscillate around the central orbit. Similar to before this will also lead to an emittance blow up due to filamentation induced by non-linear effects.

In order to minimize the required hardware parameter of the septum and the kicker like kick strength and septum thickness, the β-function at both the septum β_{septum} and at the kicker β_{kicker} should be matched to the highest feasible values. This can be seen from the following Equation [39]

$$\Delta x'_{kicker} = \frac{\Delta x_{kicker}}{\sqrt{\beta_{kicker}\beta_{septum}}\sin(\Delta\mu)}, \tag{4.8}$$

where $\Delta x'_{kicker}$ is the required angular deflection by the kicker, Δx_{kicker} the separation of the beams and $\Delta\mu$ the phase advance between the kicker and septa. From Equation (4.8) it can also be seen that a phase advance of $\Delta\mu = 90°$ between kicker and septa is advantageous when trying to reduce the required kicker strength. Additionally, a vanishing dispersion in the injection channel proves beneficial as an energy deviation does not lead to an increased aperture need. This allows to further increase the β-function in the kicker, thus decreasing the required kicker strength. Lastly, the phase advance in the injection plane between the kicker (MSI) and the injection protection (TDI) should also be matched to $\mu_{kicker} - \mu_{TDI} = 90°$ to ensure optimum protection efficiency [40].

4.4 Aperture and Tolerances

In storage rings, it is of utmost importance to have accurate aperture specifications of each element together with mechanical tolerances to accurately calculate the available beam stay clear and ensure sufficient beam clearance by identifying aperture bottlenecks early on. When going to higher beam energies this becomes even more critical as in this case the damage inflicted by beam losses to machine equipment becomes substantial. To calculate the available beam stay clear in the LHC the n_1 model was devised which is a setting related to the maximum opening of the primary collimator in units of the nominal beam size σ [41]. The primary collimators are the absorbers which are placed closest to beam to absorb particles with a too large transverse amplitude. The secondary and tertiary collimators, placed downstream of the primary collimators, then absorb the showers from the hadronic interaction of the beam with the primary collimator. The opening of the primary collimator n_1 itself is

$$n_1 = n_x = n_y \tag{4.9}$$

where n_x and n_y are normalized coordinates defined by [41]

$$n_x = \frac{x}{k_\beta \sigma_x} \qquad \text{and} \qquad n_y = \frac{y}{k_\beta \sigma_y} \tag{4.10}$$

where x and y are the transverse coordinates, k_β the square root of the β-beating coefficient and $\sigma_{x,y}$ the r.m.s beam size. The minimum tolerable primary aperture is specified as n_1^{spec} and every other element in the accelerator, especially the superconducting magnets where otherwise a quench could be induced, need to satisfy

$$n_1^{element} > n_1^{spec}. \tag{4.11}$$

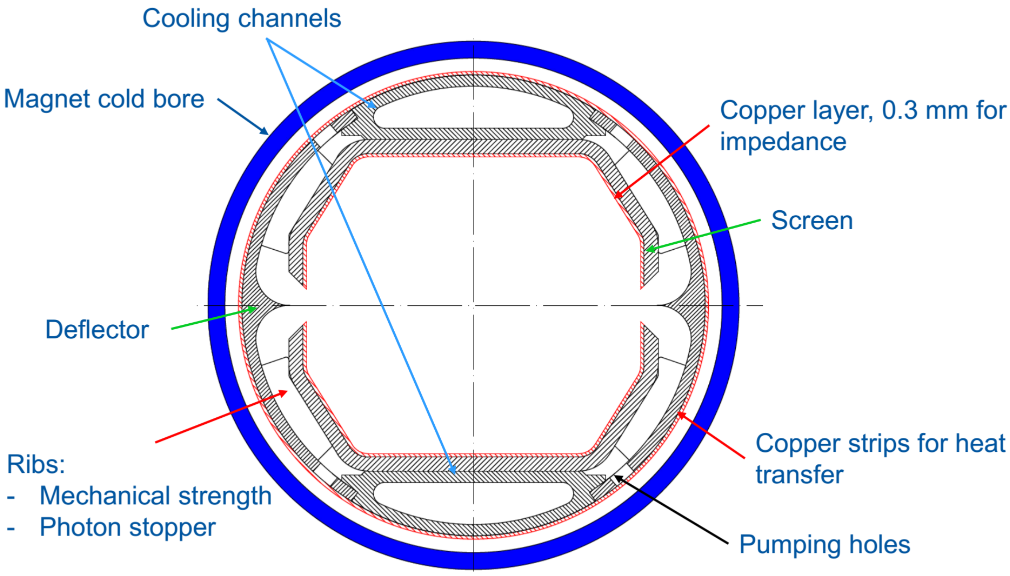

Figure 4.11: Conceptual design of the FCC beam screen and cold bore [42]

The actual aperture is given by the dimensions of beam screen. These, however, depend on a number of external factors. One of such is for example, to allow efficient removal of the heat due to synchrotron radiation by the cryogenic systems while also considering resistive wall impedance and the requirements from the vacuum pumps. The beam screen itself is then surrounded by the cooling tubes, support system, and the cold bore, illustrated in Figure 4.11.

As the gradient of the quadrupoles scales inversely with the aperture (see Equation (4.6)) there needs to be a trade-off between the outer diameter of the cold bore and the quadrupole gradient. On top of that the quadrupoles of the final focusing system in the experimental insertion require an absorber in the aperture to protect the magnets from quenches due to the deposited energy from the interaction debris. This reduces the available aperture even further. In addition, also the mechanical tolerances of the alignment of each element and errors due to ground motion need to be considered when calculating the available beam stay clear.

From the aperture standpoint, the injection optics and the collision optics pose the most challenging cases. For the collision optics, β^* is matched to the minimum feasible value to ensure maximum possible instantaneous luminosity. This consequently requires the β-functions in the triplets to be as large as possible making the triplet the aperture bottleneck. As the emittance at injection energy is significantly larger (see Equation (3.26)) the beam size for the same β-function is also significantly larger, therefore, requiring a rematching of the triplet to a higher β^*. As the arc optics remains unchanged between injection energy and top energy usually the arc section becomes the aperture bottleneck whereas other insertions can be rematched to provide sufficient beam stay clear.

4.5 Energy Deposition studies

As mentioned in the previous sections a special absorber in front of and inside quadrupole magnets of the final focusing triplet are required. These shield the magnets against the debris coming from the interaction point as the deposited energy could otherwise quench the superconducting magnets. Thus to determine an adequate absorber thickness, studies with a particle transportation and interaction code such as FLUKA [43, 44] (with DPMJET-III as event generator [45]) are necessary. From these simulations, a given shielding thickness and instantaneous luminosity the peak power density in the coils can be obtained. This, in turn, allows determining a maximum feasible instantaneous luminosity for a given power density limit, which depends amongst others on the used conductor. Similarly, the components in the magnets degrade over the operation time and should be replaced after a certain dose is accumulated. This radiation load limit sets an upper limit on the integrated luminosity. However various ways exist to partly mitigate this problem. One is the option to invert the crossing plane on a regular basis to even out the spatial energy deposition distribution [46]. Another mitigation strategy foresees splitting the first quadrupole of the triplet (Q1) in two magnets with individual aperture and absorber thickness which results in a significant reduction of the peak dose [47].

CHAPTER 5

Optics design for the Low Luminosity Experiments

5.1 Layout changes in the FCC-hh

As in the (HL-)LHC, the design of FCC-hh also foresaw from the beginning the inclusion of four experimental insertions. Two of those will house general purpose, high luminosity experiments meant to complement each other as ATLAS and CMS do in the LHC. General purpose detectors are designed to detect a wide range of particles and its decay products which allows looking at various aspects of the particle collisions. On the other hand, the other two experiments are designed as more specialized experiments conducting more specific physics studies. An example from the LHC would be the LHCb experiment which specializes on the decay of particles containing beauty-quarks. The detector was therefore specially designed to filter out these particles and their decay products.

From the beginning, the high luminosity experiments in the FCC-hh were placed exactly opposite of each other. This ensures that both experiments see the same number of collision in a given filling scheme and the mitigation of detrimental PACMAN effects [48]. The low luminosity experiments, on the other hand, were initially housed in dedicated experimental insertion in Points F and H [49]. Due to their position these experiments see a smaller number of collisions which in turn reduces the instantaneous luminosity compared to the main experiments. The first layout developed for the FCC-hh is presented in Figure 5.1.

In this layout, the straight sections for all experimental insertion are 1.4 km long whereas the so called extended straight section in points D and J are 4.2 km long and were designed to house betatron-collimation and extraction for one beam and the momentum collimation for the other beam. However, as part of civil engineering

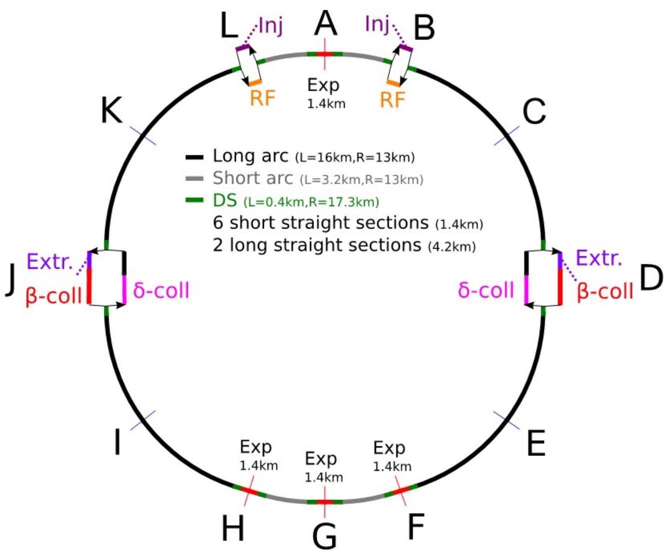

Figure 5.1: First FCC-hh layout with a circumference of 100.12 km. The high luminosity experiments are located in points A and G. Left and right of point G lie the straight sections intended for the low luminosity experiments.

optimization works conducted by CERN to reduce the cost of excavating the tunnel a new layout was proposed [50]. Part of the optimization studies aimed to reduce the shaft depth the experimental cavities. Other optimization goals were to maximize the tunnel portion in the Leman basin sedimentary rock and avoid limestone and water bearing moraines to avoid water ingress. Compared to the old layout this new layout, illustrated in Figure 5.2, has a smaller circumference of just 97.75 km. The reduction was achieved by shortening the extended straight section from 4.2 km to 2.8 km. This truncation entailed the separation of the previously combined betatron collimation and extraction sections and necessitated the reallocation of several insertions. The separation of the two systems also solved a potential problem of showers from collimation hitting the extraction kicker electronics possibly leading to an increased risk of spontaneous triggers. In the new layout, the extraction for both beams is now located in the same 2.8 km long extended straight section in point D whereas the betatron collimation is now housed in the opposite extended straight section in point J. The low luminosity experiments were moved to points B and L and are now combined with the injection insertion. Compared to the previous locations, the shaft depth to the experimental caverns is thereby significantly reduced. The straight section previously occupied by the low luminosity experiments will now house the RF-insertion and the momentum collimation insertion respectively.

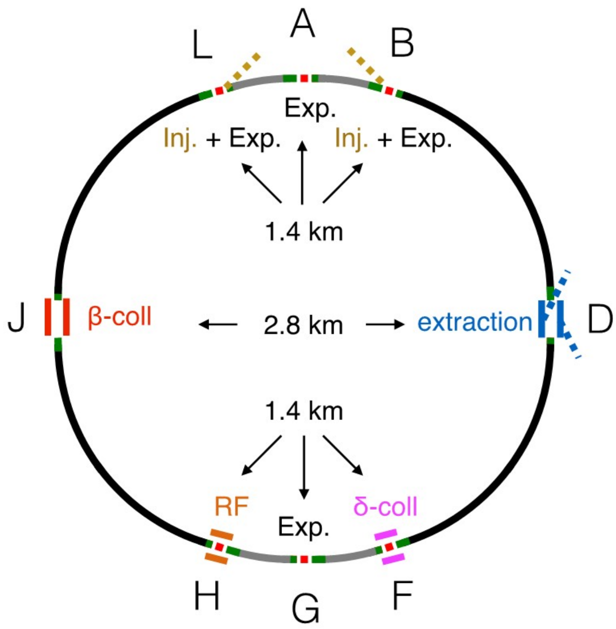

Figure 5.2: Updated FCC-hh layout with a reduced circumference of 97.75 km. Compared to the previous layout, the low luminosity experimental insertions were relocated to points B and L .

5.2 Design strategy

The new FCC-hh layout resembles the layout of LHC, where also both low luminosity experiments are combined with the injection. One of these insertions is illustrated in Figure 5.3. In these designs, the injected beam coming from the transfer line passes the septum (MSI) which is placed between Q5 and Q6. The kickers (MKI) are located in the next cell whereas the injection protection absorber (TDI) is located in between the superconducting dipoles of the separation section. This, in turn, makes the separation dipole (D1) the most exposed magnet in case of a beam impact on one of the TDI jaws. However, this design also facilitates quenches due to misinjected beams in D1 and the subsequent triplet quadrupoles as well as also possibly inducing damage to detector system. Such a case happened in the LHC for example on the 28th of July 2011 where due to an MKI-erratic 176 circulating bunches were miskicked [51, 52].

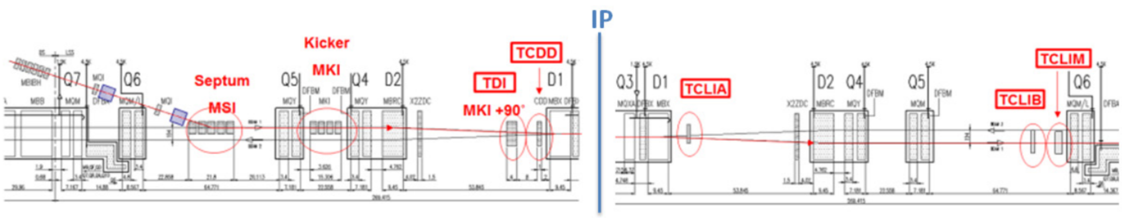

Figure 5.3: Design of the combined experimental and injection insertion for IR2 in the HL-LHC [53]

Due to such accidents concerns were raised during the initial design phase of the combined injection and experimental insertion for the FCC-hh. As the injection energy is set to increase to 3.3 TeV (with an option being studied of an injection energy of 1.3 TeV [54]) the impact of injection failures has to be studied carefully. Still, it was decided that for the first baseline designs a safe approach should be chosen. This safe approach foresees to place the injection point as far away from the experiment as practicable, a design not as deeply interwoven as the LHC insertion design. This, in turn, allows putting several protection elements between the kicker and the experiments aiming to mitigate the possible damage caused by miskicked bunches. Hence the resulting layout of the insertion is asymmetric with respect to the interaction point.

Furthermore, the optics design for the experiments does currently not favor any specific experimental scenario like a heavy-ion experiment like ALICE in the LHC or a proton-electron experiment as it is proposed by the FCC-he study group. For this universal design, a distance from the IP to the first triplet quadrupole (L^*) of 25 m was suggested by the detector design group to house a viable detector system [55]. For the baseline layout, this design will be used in both low luminosity insertions.

5.3 Initial Design Iteration

The injection of beam 1 takes place in Point B, which is why first layout were only developed for this insertion. Due to the injection, there are additional constraints on the optics in this insertion compared to Point L. It was therefore assumed that due to this, a viable design for Point B should also work in Point L with only some rematching required. Furthermore, in the following on the optics for Beam 1 are examined as no arc layout for beam 2 was available at the time of writing this thesis. When developing such insertion, one usually starts by investigating the two most demanding cases. These are the so called collision optics at top energy and the injection optics at injection energy. The collision optics is of special interest as the beam size in the IP is minimal and from this a first estimate of the expected instantaneous luminosity can be given. Also at top energy the gradients of the magnets are at their maximum which allows determining hardware requirements. The injection optics on the other hand is critical not only for determining the minimal feasible injection energy by physical and dynamic aperture studies but also allows to investigate, for example, injection failure cases.

As a starting point for this new combined insertion, it was assumed that half of the 1.4 km long insertion should be occupied by the injection hardware and the other half by the experiments. Therefore, this leaves a distance of 350 m from the interaction point to the beginning of either the dispersion suppressor or the injection part for the experiments.

Due to the constrained space, a new triplet layout has been designed with an overall length of just 77 m for the suggested L^* of 25 m. For the separation section, the magnet design presented in [56] was chosen as it achieves the required beam separation of 250 mm after a separation length of 100 m. The matching section is 150 m long and four

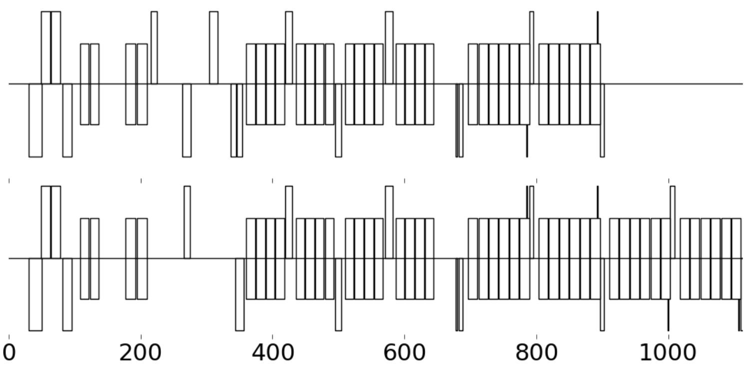

Figure 5.4: Comparison between different matching section, top: First design with four matching quadrupoles, bottom: matching section with only two matching quadrupoles and FODO cell of the ensuing arc.

matching quadrupoles were inserted with equal space between them. This first layout is illustrated in Figure 5.4 top. However, for this layout, no solution could be found which matches the predefined initial conditions in the IP and the optics constraints induced by the arc without exceeding the first estimated magnet gradient limits of 400 T/m for the matching quadrupoles. The initial conditions of $\beta^*_{x,y}$ in the IP were varied from 3 m up to 10 m with the other optics parameters $\alpha_{x,y}$ and D_x, D'_x set to zero and assuming a beam energy of 50 TeV. For matching all quadrupoles in the insertion, the first three quadrupoles of the dispersion suppressor and the three trim quadrupoles next to ensuing three quadrupoles were used. It was concluded that the lack of space between the matching quadrupoles was the main issue with this design and alternatives were investigated. The removal of two quadrupoles from the matching section and using the trim quadrupole of the first FODO cell from the ensuing arc for matching proved to be a viable solution. With an assumed β^* of 3 m as a conservative starting point, a solution matched to the arc constraints could be found. The resulting layout is presented in Figure 5.4 bottom.

It should be noted that in both layouts the same number of individually powered quadrupoles was used for matching. This layout was then used as a basis for a first combined design of injection and experimental insertion. With the layout of the injection part of the insertion provided by FCC-hh Injection group [57] a first combined layout, which is presented in Figure 5.5, has been developed and matched to the arc constraints.

The provided injection part is significantly shorter than the previously intended 700 m and consists only of three cell with each being 150 m long. This allowed putting more space between the matching quadrupoles on the left side of the IP compared to the right side. Furthermore, in this design additional injection protection elements could be placed in the four cells downstream of the TDI if deemed necessary. However, the use of additional protection elements will also put more constraints on the optics and therefore no such elements were included in these first layouts. The matching of the different optics for the insertion was conducted in two steps. Instead of matching the insertion as a whole the matching was split up in matching from the IP to the right

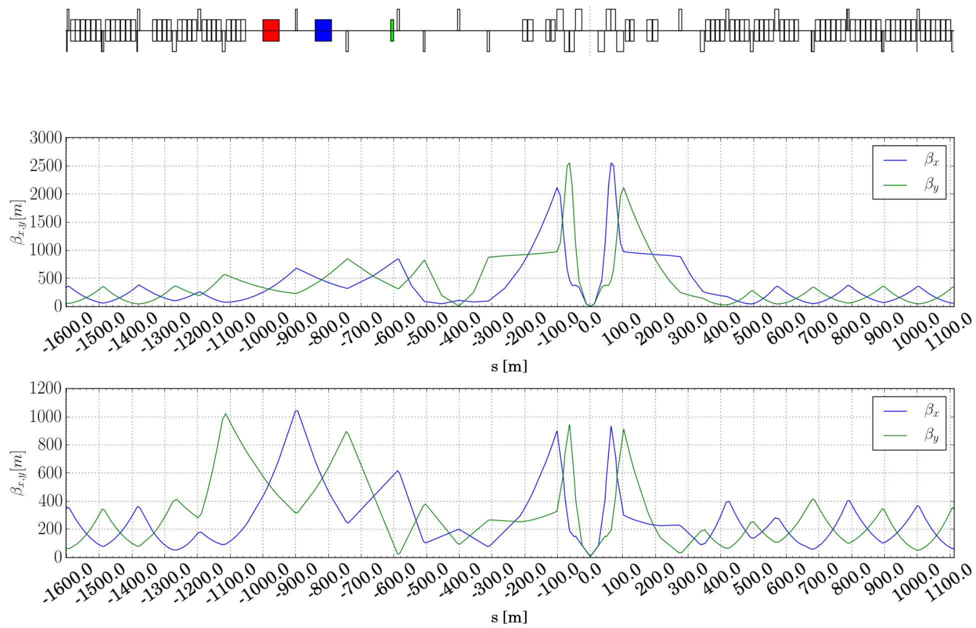

Figure 5.5: First design of a combined injection and experimental insertion for the FCC-hh. In red the position of the septum (MSI), in blue the injection kickers (MKI) and in green the injection protection (TDI), top: top energy of 50 TeV and β^* of 3 m, bottom: injection energy of 3.3 TeV and β^* of 8 m

dispersion suppressor and from the IP to the left dispersion suppressor. Compared to matching the complete insertion by providing starting condition on the left side and constrain the optics in the IP and on the right-hand side this approach should ensure a faster convergence of the matching algorithm as it involves fewer variables. For matching the collision optics the right-hand side was matched first as it has offers fewer degrees of freedom due to the smaller number of individually powered quadrupoles. The injection side was then also matched from the IP to the arc by providing the initial conditions for the IP. The triplet quadrupoles were not used for matching and instead the gradients from the matched right-hand side were taken. For matching the optics to the arc, all quadrupoles in the matching section, the first three quadrupoles from the dispersion suppressor and the trim quadrupoles next to ensuing quadrupoles were used.

However, the matching of the injection energy optics required a different approach. Contrary to the collision optics matching, here the injection side of the insertion is matched first as it is more constrained. In addition, the injection side was matched starting from the end of the dispersion and not from the IP. The insertion is matched so that the dispersion vanishes between the septum and the kickers. However, the separation and recombination dipoles between the injection hardware and the IP introduce a non-zero dispersion at the IP. The insertion part was therefore matched starting from the arc side and with no constraint on D_x and D'_x at the IP. The resulting optics functions at the IP were then saved and used as initial conditions at the IP when matching the non-injection side. Opposed to the collision optics the identical powering of left and right-hand triplet quadrupoles is not mandatory.

In addition to the optics also the orbit has to be matched using the orbit corrector inside and after triplet so that the beams collide under a predefined crossing angle. The crossing angle in the low luminosity experiments is determined by $\theta = \sqrt{\frac{\epsilon_N}{\gamma\beta^*}}n$ where n is the so called half-crossing angle in units of beam sigma. For these insertions, it was determined by scaling down the half-crossing angle $n_{highLumi} = 7.6$ [58] from the high-luminosity experiments via

$$n_{lowLumi} = \sqrt{\frac{D^{lowLumi}_{IP->D1}}{D^{highLumi}_{IP->D1}}} n_{highLumi} \tag{5.1}$$

where $D^{lowLumi}_{IP->D1}$ and $D^{highLumi}_{IP->D1}$ are the distances between the interaction point and the separation dipole in the low luminosity experiments and the main experiments respectively. With this scaling $n_{lowLumi} = 5.25$ was obtained which corresponds to a half-crossing angle of 19.48 µrad for a β^* of 3 m. The scaling law is derived from Equation (3.58) and keeping the long range beam-beam tune shift ΔQ_{lr} equal for the both systems. However careful tracking studies taking into account the beam-beam interaction in all experiments are necessary to determine a safe crossing angle.

In the non-crossing plane, the beam orbit also has to be matched to provide sufficient beam separation when not in colliding mode. For the beam separation, the same value of $d = 1.5$ mm as in the high luminosity experiments is used. This is equivalent to 20 σ for an injection energy of 3.3 TeV and a β^* of 8 m. The crossing schemes for Point B for both separation and crossing bumps is presented in Figure 5.6.

Following the matching of the beam optics and the orbits, the n_1 values for all elements are calculated using the APERTURE module in MAD-X. This was done to ensure that the beam stay clear value in all elements is above the minimum required n_1 of 15.5 σ [59]. The insertion is rematched if the beam stay clear is below the target value in an element and if necessary the β^* is increased. The used parameter for the aperture calculation are presented in Table 5.7a. Using the halo extension parameter indicated in [60] allows to calculate the beam stay clear in units of beam sigma.

For the aperture of triplet quadrupole a simple model, already used for the triplet quadrupoles in the main experiments [61], was used. The inner coil diameter d of these magnets is calculated with

$$d = 2\frac{B_{peak}}{G} \tag{5.2}$$

where B_{peak} is the peak magnetic field in the coil and G is the quadrupole gradient in T/m. The peak magnetic field B_{peak} is assumed to be 11 T and independent of the required gradient. The inner coil diameter is then further reduced by various inlays like the cold bore or the absorber to protect the magnets against the collision debris. The various layers with the respective thicknesses are presented in Table 5.7b and are similar to the ones used in the high luminosity experiments. Compared to the main experiments

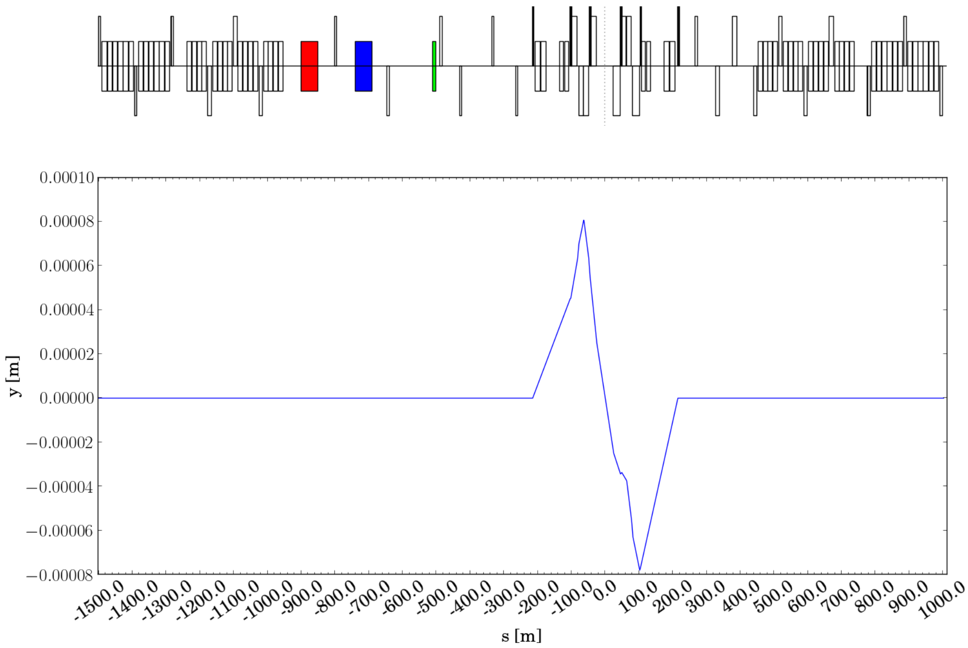

(a) Horizontal crossing bumps for Beam 1

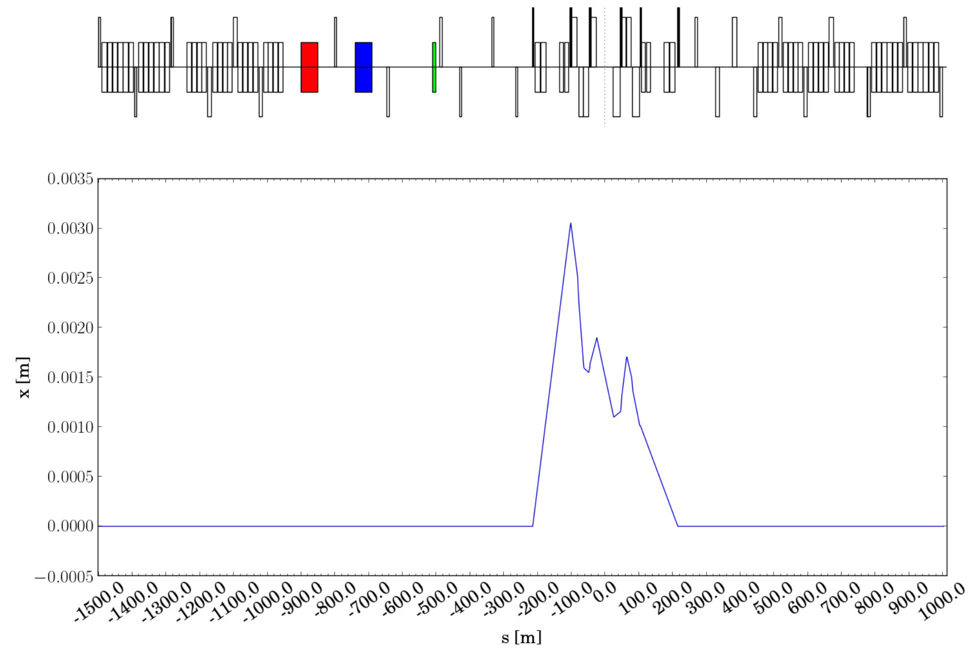

(b) Vertical separation bumps for Beam 1

Figure 5.6: Separation and Crossing Bumps in Point B for Beam 1. Indicated in black are the nested corrector dipoles.

Normalized Emittance ϵ_N	2.2 µm
Closed Orbit uncertainty	4 mm
Momentum offset	$6 \cdot 10^{-4}$
β - beating coefficient	1.1
Relative parasitic dispersion	0.14

(a) Inputparameters for the Aperture calculations in MAD-X [62]

Shielding	10 mm
Liquid Helium	1.5 mm
Kapton Insulator	0.5 mm
Cold Bore	2 mm
Beam screen	2.05 mm
Beam screen insulation	2 mm

(b) Assumed thicknesses of the layers reducing the aperture in the triplet quadrupoles

Table 5.7: Parameters for the free aperture calculations

only the shielding thickness was reduced from 15 mm to 10 mm as less debris was expected due to the lower instantaneous luminosity. However, energy deposition studies are required at one point to determine if the chosen absorber thickness is sufficient.

For the dipoles in the separation section, a circular aperture was chosen, in the case of the separation dipole with a diameter of 100 mm and for the recombination dipole with a diameter of 60 mm. The aperture follows suggestions from [56] as in these magnets the crosstalk could become an issue. To avoid this, the aperture should be as small as possible to provide sufficient space between the beam pipes. As the separation dipole is a single aperture dipole the feasible aperture is less of an issue and was tentatively increased to provide space for shielding if necessary. For the matching quadrupoles a rectellipse aperture type was chosen, as this closely resembles the real shape of the FCC-hh beam screen. The rectellipse shape is an intersection of an ellipse and a rectangle as illustrated in Figure 5.8b.

The beam screen aperture was increased in the matching quadrupoles Q4 and Q5 on the right-hand sides and also in the quadrupoles Q8 and Q9 on the injection side. The reason is a higher expected β-function due to either the injection phase advance constraint or due to the high β-function in the triplet not yet being brought down to acceptable levels. The used dimensions are summarized in Table 5.1 and the results of the aperture calculations are presented in Figure 5.9.

The results show that while the beam stay clear during collision is significantly above the requirements, during injection the beam stay clear in the triplet is just slightly above 15.5 σ. The inclusion of misalignments of the quadrupoles will reduce the beam stay clear even further and as a result the β^* at injection will likely have to be increased. For collision optics, the overabundance of beam stay clear would allow to either decrease β^*, increase the shielding thickness, or increase the crossing angle depending on the preferred scenario for the experiments.

Due to the injection part of the insertion being significantly shorter than previously assumed, alternatives to the presented design were investigated. The studies aim to use the extra space to shorten the injection side and extend the matching section on the non-injection side to four matching quadrupoles again. The resulting design would not require the use of the arc FODO-cell for matching.

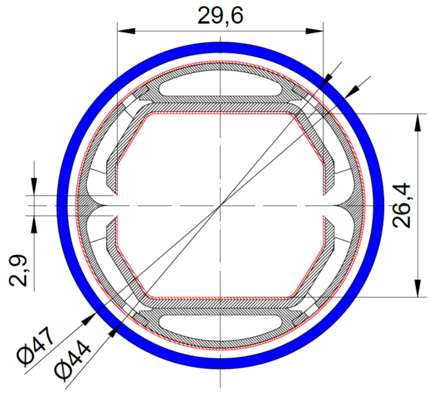

(a) FCC-hh beamscreen and dimension [42]

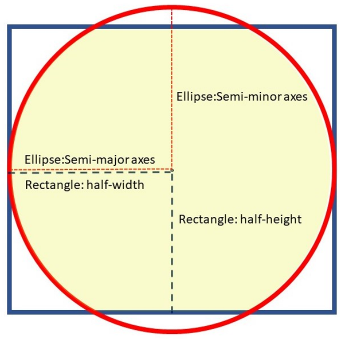

(b) Intersection of a ellipse and a rectangle forming a rectellipse shape in yellow

Figure 5.8: Comparison between the FCC-hh beamscreen and the rectellipse shape, used for aperture calculation ins MAD-X

Aperturetype	**Dimension** [m]	**used in**
Rectellipse	0.015, 0.0132, 0.015, 0.015	DIS quadrupoles and dipoles, Q4L, Q5L, Q6L, Q7L
Rectellipse	0.0289, 0.024, 0.0289, 0.0289	Q4R, Q5R, Q8L, Q9L, MKI, MSI
Circle	r = 0.05	D1L, D1R
Circle	r = 0.03	D2L, D2R
Circle	r = 0.018	Q1L, Q1R
Circle	r = 0.0185	Q2L, Q2R
Circle	r = 0.027	Q3L, Q3R

Table 5.1: Shape and dimensions of the free aperture in the magnets. In case of the rectellipse, the presented values are the half width and half height of the rectangle, followed by the horizontal and vertical semi-axes of the ellipse.

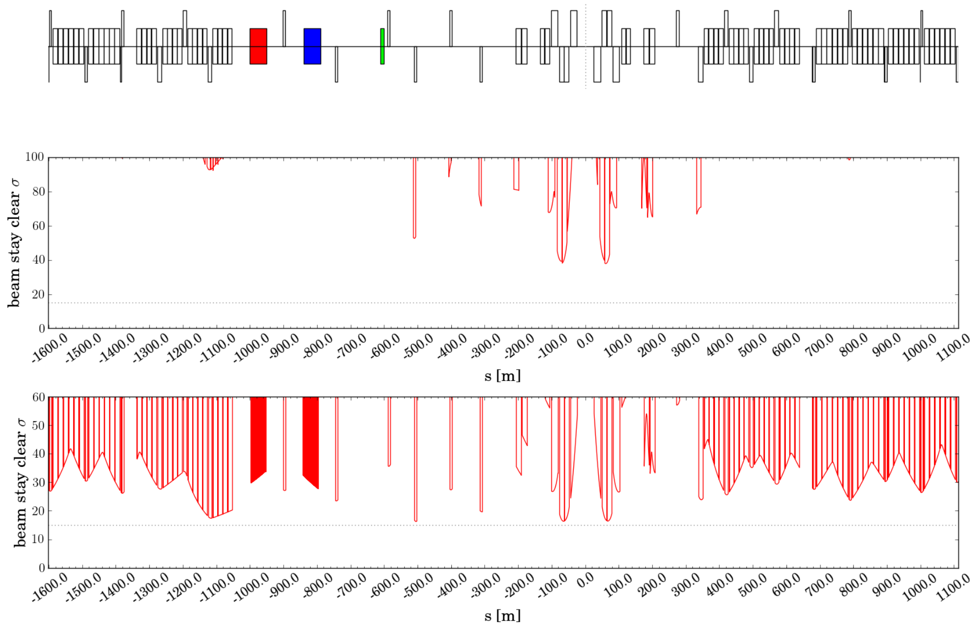

Figure 5.9: Calculated beam stay clear values for both collision and injection optics. The minimum tolerable n_1 level of 15 σ is marked with a gray line. top: collision, bottom: injection

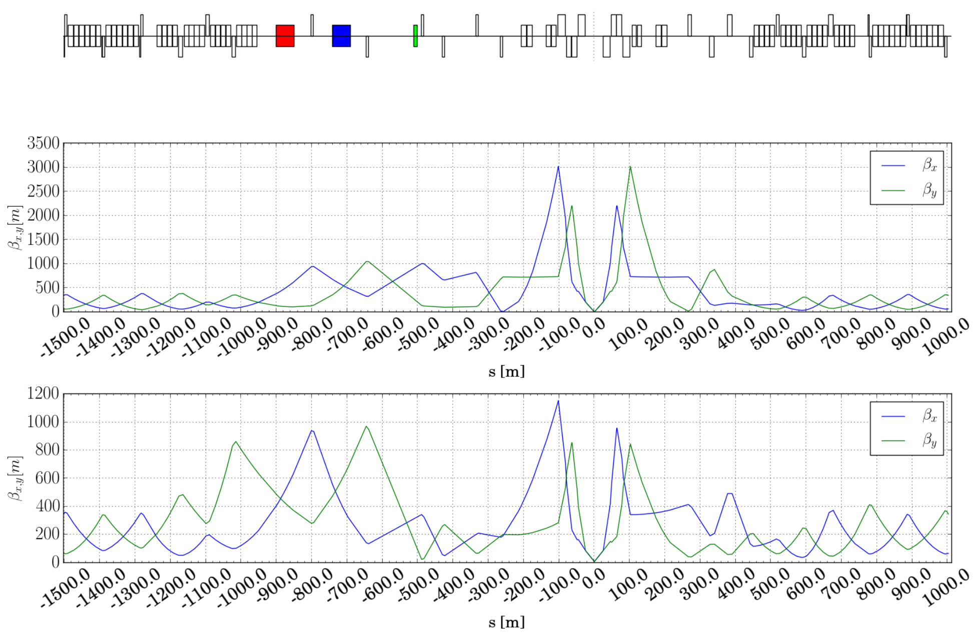

Figure 5.10: Optimized design of a combined experimental and injection for the FCC-hh. In red the position of the septum (MSI), in blue the injection kickers (MKI) and in green the injection protection (TDI), top: 50 TeV and β^* of 3 m, bottom: injection energy of 3.3 TeV and β^* of 8 m

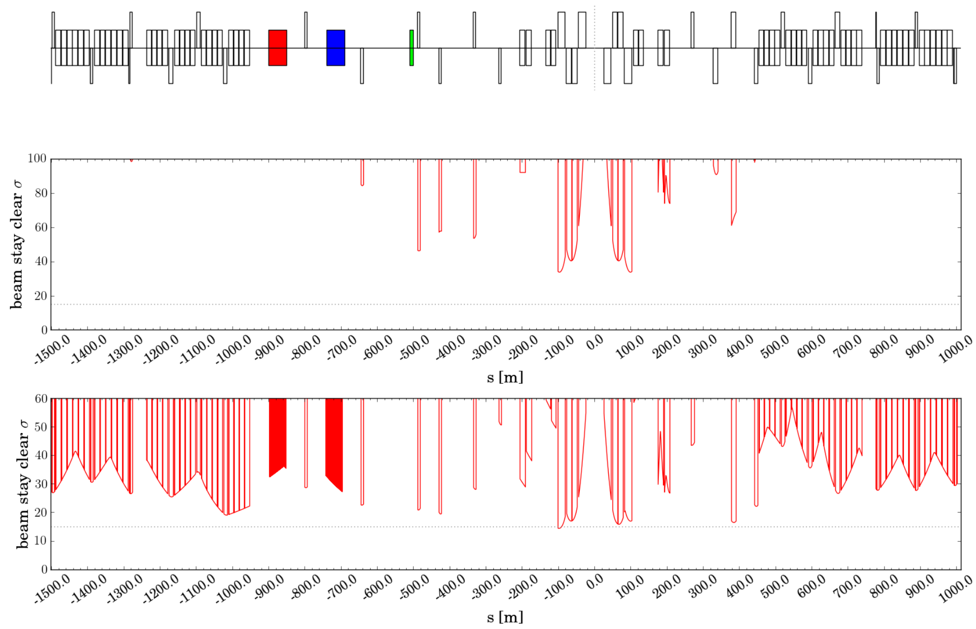

Figure 5.11: Calculated beam stay clear values of the new combined experimental and injection insertion for both collision and injection optics. The minimum tolerable n_1 level of 15 σ is marked with a gray line. top: collision, bottom: injection

By moving the IP 100 m to the left side, a solution for matching the arc constraints on both sides could be found. The resulting new layout is presented in Figure 5.10. Both L^* and β^* were kept the same between both designs. During the rematching of the collision optics the gradients in the triplet changed significantly. As the strength of Q2 in this design is higher than Q1, the free aperture of Q2 is also smaller than the free aperture of Q1. This however is unfavorable from an energy deposition stand point. In this case Q2 would act as a bottleneck and would be exposed to more radiation [63]. To circumvent this, a uniform coil aperture for the triplet quadrupoles was used instead. Due to this rematching and the new aperture dimension for the triplet quadrupoles the minimum beam stay clear during collision decreased by 5 σ and the position of the bottleneck moved from Q2 to Q3. The beam stay clear value now is 34 σ. For the injection optics, the loss amounts to about 1 σ.

Based on this layout, the other low luminosity insertion in Point L was developed. The layout from Point B has been inverted and the polarity of each quadrupole needed to be inverted as well due to inverted arc constraints. Both the L^* of 25 m and β^* during collision and injection were kept. Furthermore, the triplet gradients for the collision optics remain the same as in Point B. The final matched optics for the insertion is presented in Figure 5.12. As Beam 2 is injected in Point L, the presented optics for Beam 1 does not include the equipment such as kickers and septa. Additionally, during matching the injection optics, no additional phase advance constraints had to be taken into account. Due to the large spacing between Q7, Q8, and Q9, the β-functions there are quite sizable. This bump could not be reduced by rematching with additional constraints. To provide sufficient beam stay clear in Q7, the aperture had to be increased in this quadrupole. The results of the aperture calculations for insertion in Point L with

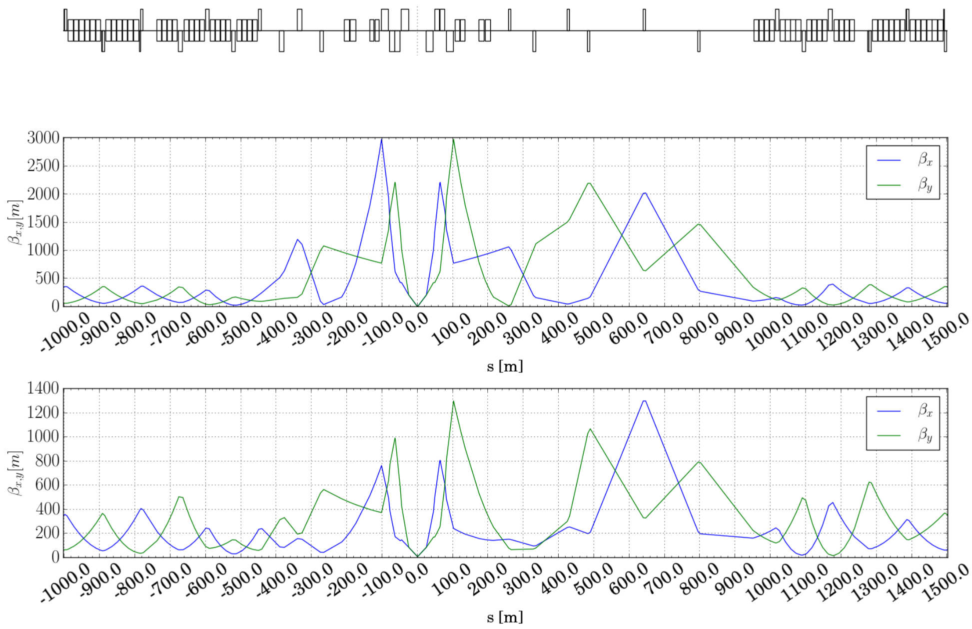

Figure 5.12: Optical functions for the low luminosity insertion in Point L , top: top energy of 50 TeV and β^* of 3 m, bottom: injection energy of 3.3 TeV and β^* of 8 m

the modified Q7 aperture are shown in Figure 5.13.

Together with the previously presented design for Point B, these two layout present first practicable low-luminosity experimental insertions and were integrated into the FCC-hh lattice [64] for further studies.

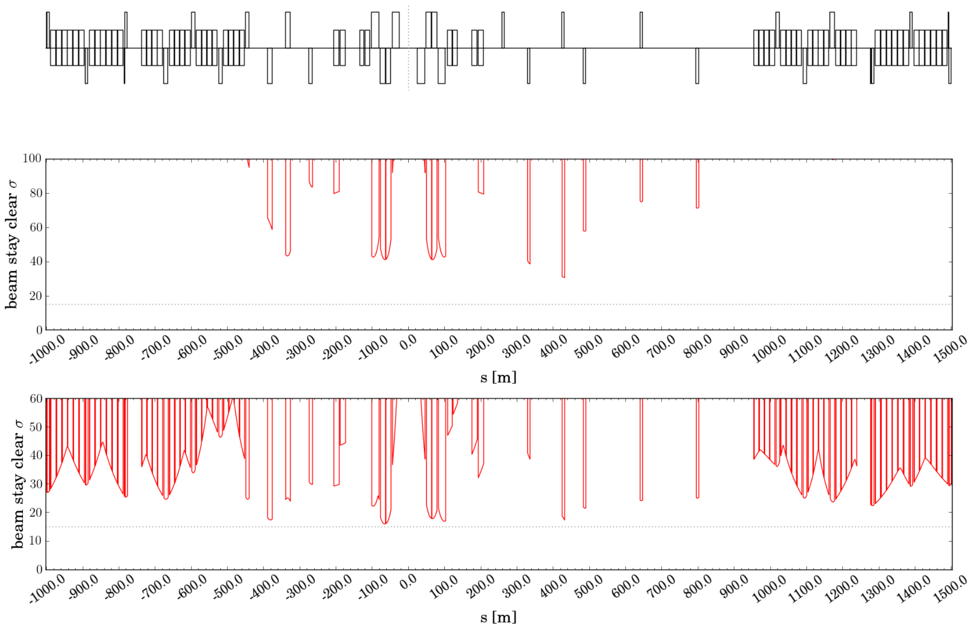

Figure 5.13: Beam stay clear values for both collision and injection optics. The minimum tolerable n_1 level of 15 σ is marked with a gray line. top: collision, bottom: injection

5.4 Split quadrupole models

First insights provided by the magnet group indicated that the simple model for the triplet quadrupole apertures was indeed rather optimistic for the required quadrupole gradients [65]. For the required gradient of 270 T/m an inner coil radius of 32 mm was suggested instead of the 40 mm coil radius obtained via Equation (5.2). Additionally the longest feasible magnet has been defined as 15 m. Due to this new requirement, the previously 20 m long quadrupoles Q1 and Q3 needed to be split. As these new, separated quadrupoles are housed in separate cryostats, a gap of at least 2 m had to be inserted. Both the new aperture model and the splitting of the triplet quadrupoles pose substantial changes to the previous design. In the new design with the split quadrupoles, the separation section was moved back by 5.5 m to provide space for the split quadrupoles.

In addition the intra-beam-spacing of previously 250 mm has also been reduced. The new intra-beam-spacing of 204 mm [66] mainly affects the dipoles in the separation sections. This change allows to either keep the dipole field strength constant and decrease the length of the separation section or decrease the dipole field instead and keep the distance between the dipoles constant. For the new design, the second option was chosen as only 12 m could be gained with the first option. With the second option however, the field in D1 decreases from 12 T to 10 T and in D2 from previously 10 T to 8 T. Especially with the recombination dipole D2, these seemed the better solution as the electromagnetic cross talk and therefore magnetic errors should be reduced. However, careful magnetic field studies are required to confirm this. Furthermore,

Type	**Coilaperture [mm]**	**Gradient [T/m]**	**Field [T]**	**Length [m]**
Triplet Q1	64	270	-	10
Triplet Q2	64	270	-	15
Triplet Q3	64	270	-	10
Separation Dipole D1	100	-	10	12.5
Recombination Dipole D2	60	-	8	15
Matching Quadrupole Short	70	200	-	9.1
Matching Quadrupole Long	50	300	-	12.8

Table 5.2: Overview over the used magnet families

for this new design the specifications for the matching quadrupoles were harmonized and now the same two types of matching quadrupoles as in the main experiments are used. A complete list of the magnet families used in the new insertion is presented in Table 5.2.

The significant reduction of free aperture in the triplet quadrupoles required the revalidation of the chosen β^* for collision and injection. For the β^* of 3 m during collision, the decrease of coil aperture resulted in a loss of about 10 σ beam stay clear. However, due to large beam stay clear of 30 σ in the previous layout, the value in the updated layout is still above the required 15.5 σ and thus, the current β^* could be kept. The injection β^* on the other hand had to be increased. A solution which provides sufficient beam stay clear in the triplet was found for a β^* of 27 m.

During the initial matching of the updated layout, no solution for the injection optics for Insertion L could be found with sufficient beam stay clear. Especially the region between Q9 and the first quadrupole in the dispersion suppressor on the left-hand side was prone to excursion of the β-function leading to aperture problems. It was assumed that the reason for this was the large distance between the last quadrupole of the matching section and the dispersion suppressor. Therefore, a new design was developed with a slight rearrangement of the matching quadrupoles in the longer part the insertion. The new layout for insertion B together with the collision and injection optics is presented in Figure 5.14. Compared to the previous layout, the MSI, MKI, and the TDI were each moved downstream by one cell and the last quadrupole Q9 was moved closer to the dispersion suppressor. The cell length of the three cells hosting the injection hardware was kept at 150 m. As the injection elements were moved by one cell, also the polarity of the first quadrupole after the septum has changed. Therefore the injection plane in this layout changed from vertical to horizontal.

Updated parameters for the aperture calculation in MAD-X for the new layout were used and are shown in Table 5.3. Especially the reduction of the closed orbit uncertainty from 4 mm to 2 mm significantly improves the minimum beam stay clear during collision from 25 σ to 30 σ. Additionally to the new aperture parameters also a first

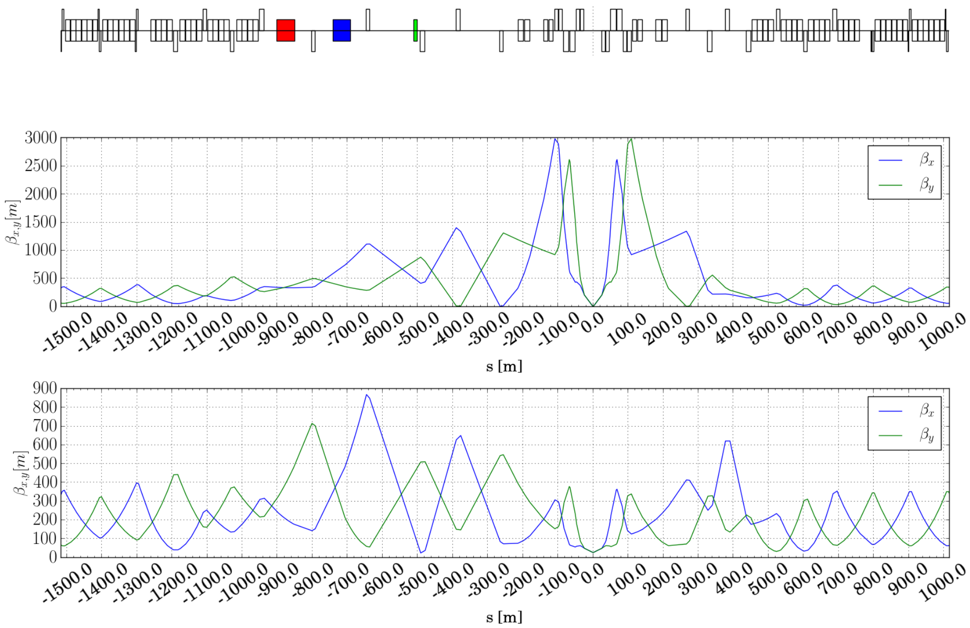

Figure 5.14: Updated layout with a rearranged matching section and split quadrupoles in the triplet. top: top energy of 50 TeV and β^* of 3 m, bottom: injection energy of 3.3 TeV and β^* of 27 m

	Injection	**Collision**
Radial closed orbit excursion	2 mm	2 mm
β - beating coefficient	1.05	1.1
Momentum offset	$6 \cdot 10^{-4}$	$2 \cdot 10^{-4}$
Relative parasitic dispersion	0.14	0.1

Table 5.3: Updated parameters for the aperture calculation in MAD-X [67]

set of mechanical and alignment tolerances for the magnets in the insertion has been considered. These tolerances for the respective magnets in Insertion B are presented in Table 5.15a, while the definition used by MAD-X are shown in Figure 5.15b

The results of the aperture calculations using the new parameters and tolerances are presented in Figure 5.16. Compared to the previous layout, the minimum beam stay clear during collision was reduced from 35 σ to 25 σ. The β^*-reach decreases therefore significantly compared to the previous layout.

As before, the new layout with the rearranged matching section and the new split triplet quadrupoles was then adapted for Point L and matched to arc. With the rearrangement of matching quadrupoles on the right-hand side of Insertion L, the previous problem with β-function excursion was solved and the beam stay clear is now well above the target. This is illustrated in Figure 5.18.

With the beam parameters presented in Table 2.1 and a matched β^* of 3 m a first attainable instantaneous luminosity can be calculated. Using Equation (4.2) and neglecting the geometric loss factor S for now one obtains a peak instantaneous luminosity $\mathscr{L}$

Magnettype	**r**	**g**	**s**
Q1	1.3 mm	1.0 mm	1.0 mm
Q2	0.9 mm	0 mm	0.6 mm
Q3	1.1 mm	0 mm	0.8 mm
D1	0.84 mm	2.36 mm	2.0 mm
D2	0.84 mm	2.36 mm	2.0 mm
Q4,Q5, Q7L, Q8L	0.84 mm	1.0 mm	1.0 mm
Q6, Q7R, Q9L	0.84 mm	1.0 mm	0.5 mm

(a) First set of alignment tolerances for the insertion magnets [68]

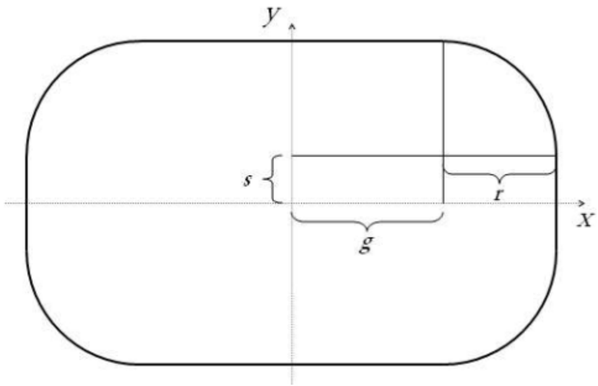

(b) Definition of the aperture tolerances in MAD-X [25]

Figure 5.15: Alignment tolerances for the insertion magnet and tolerance definition

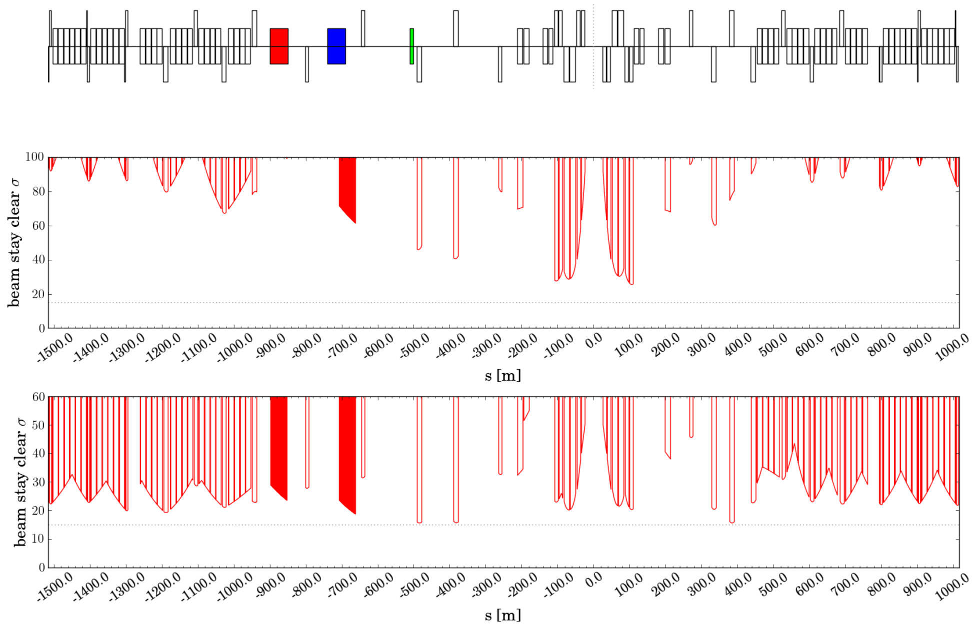

Figure 5.16: Aperture calculation results for the new layout with a rearranged matching section and new aperture parameter. The minimum tolerable n_1 level of 15 σ is marked with a gray line. top: collision optics, bottom: injection optics

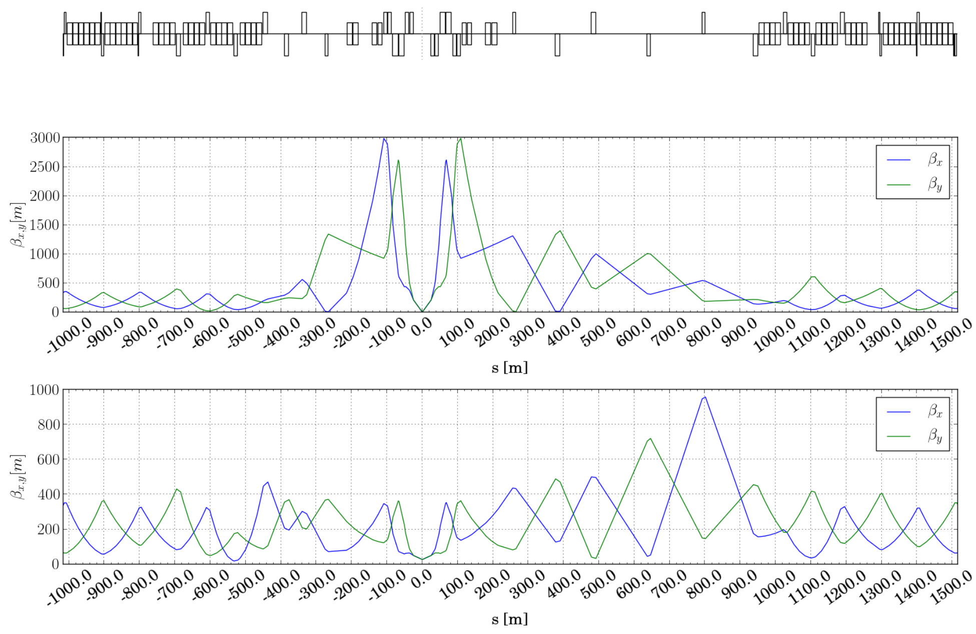

Figure 5.17: Updated layout with a rearranged matching section and split quadrupoles in the triplet for Point L. top: top energy of 50 TeV and β^* of 3 m, bottom: injection energy of 3.3 TeV and β^* of 27 m

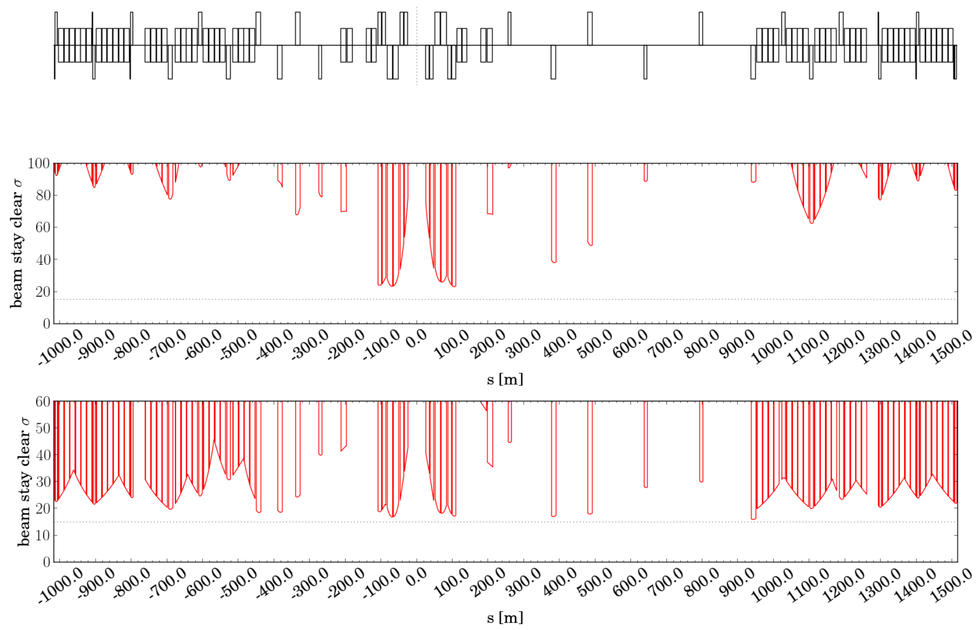

Figure 5.18: Aperture calculation results for the new layout with a rearranged matching section and new aperture parameter for Point L. The minimum tolerable n_1 level of 15 σ is marked with a gray line. top: collision optics, bottom: injection optics

of $2.09 \cdot 10^{34} cm^{-2} s^{-1}$, already twice as high as the design luminosity for CMS and ATLAS [6]. However, it should be noted that in this case the full number of bunches n_b was used for the calculation. Depending on the filling scheme in FCC-hh the low luminosity experiments will see a decreased number of colliding bunches. In the LHC for example, only 2736 and 2622 of the available 2808 bunches collide in IP2 and IP8 respectively in the nominal scheme with a 25 ns spacing [69]. The final number of possible collision and achievable instantaneous luminosity in these interaction points will depend on the chosen filling scheme, bunch spacing, and the arc lengths [70]. Using a rms bunch length σ_z of 6.8 μm [71] the geometric loss factor S is 0.9903.

Using the design developed in the framework of this thesis, various studies were carried out by other FCC-hh study group participants to investigate the feasibility of the chosen parameters and the effects on beam stability. Two of these studies together with first results shall be briefly mentioned and their impact on next design will be discussed. Lastly a possible design strategy for the next layouts will be given.

5.4.1 FLUKA studies

The first studies which shall be discussed here are energy deposition studies of the triplet quadrupoles. FLUKA studies were carried out to determine both maximum power density and peak dose. The results indicate, if the chosen shielding thickness of 10 mm is sufficient or needs to be increased. The peak power density limit has been set to 5 $mWcm^{-3}$ at this stage and the baseline radiation limit for the superconducting magnets is 30 MGy [72]. For the absorber INERMET180, a heavy tungsten allow, was chosen at this point. Additionally, an 80 cm long tungsten mask was placed in front of Q1. As all triplet quadrupoles will be housed in separate cryostats, a shielding gap in the interconnects also needs to be taken into account. At this stage, the gap was assumed to be 70 cm long. The results of these energy deposition studies are presented in Figure 5.19.

It should be noted that the assumed instantaneous luminosity in these simulations is a factor 4 below the maximum attainable luminosity. However, the results of the peak power density studies scale linearly with the luminosity, thus also allowing to draw conclusions for the peak instantaneous luminosity of $2.09 \cdot 10^{34} cm^{-2} s^{-1}$ [63]. The results in Figure 5.19a show that the chosen absorber thickness is sufficient in bringing the peak power density below the current design limit. However, it can also be seen that the peak dose occurs at the beginning of the first quadrupole. This indicates that the mask is critical for bringing down the peak power density and it should be optimized further. Also clearly visible is the effect of the unshielded gaps between the quadrupoles. The minimum feasible gap length should therefore also be investigated for following energy deposition studies.

In Figure 5.19b the peak dose in the triplet quadrupoles is shown. From this simulations, it can be seen that target radiation limit of 30 MGy is met for an integrated luminosity of 500 fb^{-1}. As was the case in the peak power density studies, also here the peak dose occurs in the beginning of the first quadrupole. This again highlights the importance of

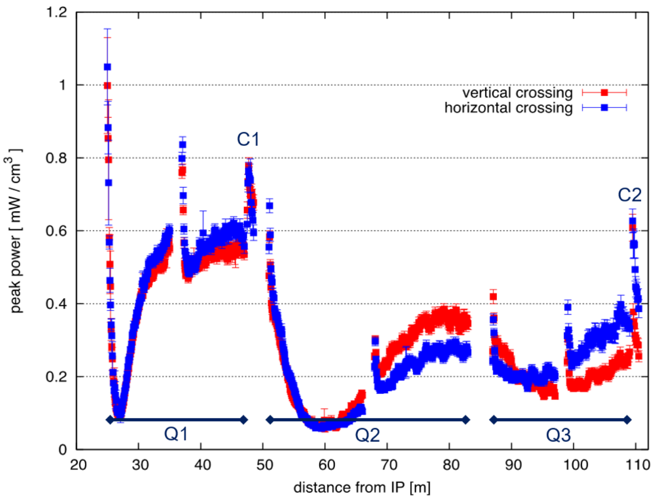

(a) Peak power density for an instantaneous luminosity of $5 \cdot 10^{33} cm^{-2} s^{-1}$

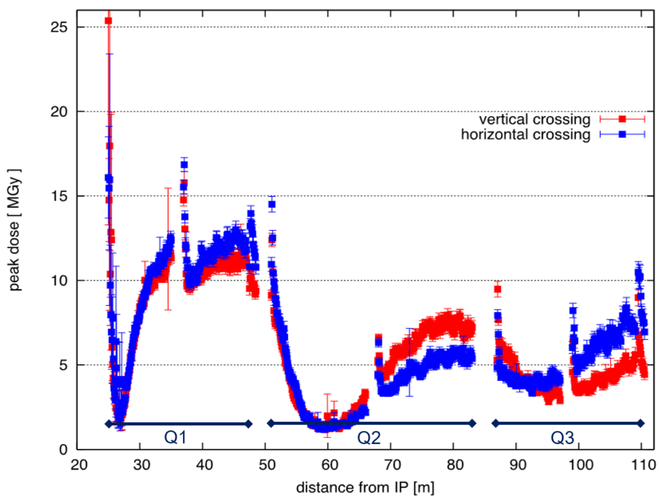

(b) Peak dose in the triplet quadrupoles for an integrated luminosity of $500 fb^{-1}$

Figure 5.19: Results from energy depositions studies with FLUKA. Courtesy of M.I. Besana and F. Cerutti

revisiting the design of the mask in front of Q1 when trying to optimize the performance of the low luminosity experiments.

5.4.2 Beam-Beam studies

From beam-beam studies first conclusions on the validity of the scaling of the crossing angle can be drawn. The half-crossing angle of 19 μrad was up to this point only based on simply scaling down from the high luminosity experiments. However, from dynamic aperture studies with only long-range beam-beam effects in both the high luminosity experiments and the low luminosity experiments presented in [73] the conclusion was drawn that the current half-crossing angle is too low. For the low luminosity experiments instead a half-crossing angle of at least 75 μrad was proposed to not interfere with the high luminosity experiments. Unfortunately, aperture calculation with this crossing angle yield a minimum beam stay clear value below the limit of 15.5σ. This, in turn, would require the increase of the matched β^* during collision in order to decrease the β-function in the triplet quadrupole if this crossing angle is to be adapted.

5.4.3 β^*-reach

In order to collide the two beams under the proposed crossing angle of 150 μrad while keeping the same β^* of 3 m a significant redesign will be needed. This redesign will center around larger aperture triplet quadrupoles to still allow for sufficient beam stay clear. This increase in aperture can also be used to either increase the shielding thickness or decreasing β^*, thus increasing the instantaneous luminosity. To increase the triplet aperture while keeping the focusing properties constant to retain the same β^*, the length of the triplet quadrupoles needs to increase. The increased demand in space by the triplet could then for example partly be recovered by shortening the cell length between Q4 and Q5 and Q5 and Q6 on the injection side. First designs using this approach studied a length increase of the triplet magnets by 40 %. This lengthening resulting in a decrease of maximum gradient from 270 T/m to 191 T/m. Using [74]

$$r = 29.96\, G^{-1.215} \tag{5.3}$$

where G is the quadrupole gradient,the new aperture for the triplet magnets has been determined. With the new inner coil diameter of 100 mm, the resulting beam stay clear in triplet is 40 σ when using a crossing angle of 180 μrad. This excess in beam stay clear could then also be used to increase the absorber thickness, thereby lowering the peak dose and allowing for more integrated luminosity.
However, it should be noted that these informal studies did not take into account all the required constraint and for example no injection optic was matched at that point. Furthermore, the implication of the longer triplet on for example chromaticity and Dynamic aperture should be studied as well before replacing the previously proposed baseline design.

CHAPTER 6

Dynamic Aperture Studies

With the introduction of sextupoles to correct chromaticity and other higher order multipoles into a linear lattice non-linear forces will act on the particle. Higher order multipoles also derive from unavoidable field imperfections from the superconducting magnets. These non-linear elements can excite non-linear resonances which in turn affect the long term stability of a particle and may lead to fast particle losses. To study this effects on the particle stability, tracking studies are required which allow to determine a region in phase space where the particle motion is stable. A short introduction to the concept of the Dynamic aperture is given at the beginning of this chapter. In the following, results of dynamic aperture studies at top energy with magnetic errors in the triplet of the low luminosity insertion are presented and discussed.

6.1 Dynamic aperture

The Dynamic aperture (DA) is defined as the maximum amplitude in phase space where the particle motion is stable. This amplitude is given in units of the RMS beam size. Particles starting within this domain are said to be confined there for a specified time frame. Conversely the oscillation amplitude of a particle starting with an initial amplitude above the DA will grow excessively and will be eventually be lost. As these losses may damage the accelerator equipment a design goal for a particle collider is to achieve a large enough DA. A sufficient DA is given if it exceeds the physical aperture of the storage ring and provides margin in case of expected additional error sources.

The dynamic aperture D is usually given for a number of turns N and scales with [75]

$$D(N) = D_\infty \left(1 + \frac{b}{\log_{10} N}\right) \tag{6.1}$$

where D_∞ is the dynamic aperture after an infinite number of turns and the constant b a measure for the long term losses. The DA is also closely related to the boundary between stable and chaotic motion. The onset of chaotic motion can be characterized by the Lyapunov coefficient λ. Starting with two initially very close particles with a separation d in phase space it is defined as [76]

$$\lambda = \lim_{d(0)\to 0, t\to\infty} \frac{1}{t} \left| \frac{d(t)}{d(0)} \right| \tag{6.2}$$

where t is the time passed or equivalently the tracked number of turns. A chaotic motion is characterized by a positive Lyapunov coefficient.

6.2 Magnetic Field errors

One of the factors determining the DA in the LHC for the collision optics were the field imperfections in the triplet quadrupoles and separation dipoles.

Using the LHC convention for multipole expansion the general magnetic field is given by [77]

$$B_y + iB_x = \mathscr{B}_N R_{ref}^{N-1} \sum_{n=1}^{\infty} (b_n + ia_n) \left(\frac{x + iy}{R_{ref}} \right)^{n-1} \tag{6.3}$$

where n gives the order of the multipole. For example, a coefficient with n=1 is the dipole coefficient and with n=2 a quadrupole coefficent. N marks main component of the given magnet. $\mathscr{B}$ is the normal coefficient of the given magnet in Tm^{1-n} which in case of a quadrupole (N=2) is the quadrupole gradient. R_{ref} is the reference radius and the coefficients b_n and a_n represent the normal and skew relative field errors at the the reference radius. These coefficients are unit-less and are usually given in units of 10^{-4}. Each coefficient composes of three components, the systematic error (s), the error in the same production line (u) and a random error (r) [33]. The coefficient is then written as

$$b_n = b_{n_s} + \frac{\xi_u}{1.5} b_{n_u} + \xi_r b_{n_r} \tag{6.4}$$

where ξ_u and ξ_r are gaussian distributed random numbers with the distribution truncated at 1.5 and 3 σ respectively.

In addition to this field imperfections, a beam passing through the magnet with a transverse displacement to the magnetic axis also experiences fields in all lower orders. This so-called feed-down effect lets for example an off-center sextupole also generates a dipole and a quadrupole field. These then in turn affect lattice functions such as the closed orbit and the tune. Due to the crossing angle the beams pass through the triplet off-center making them susceptible to this feed-down effect.

Turns	10^5
Number of Seeds	60
Normalized emittance ϵ_N	2.2 μm
Energy	50 TeV
Tune	111.31, 109.32
Chromaticity	2
Relative momentum spread dp/p	0.00027
Amplitude step size	2 σ
Particle pairs per step	30
Angles in x-y plane	5

Table 6.1: Parameters for the SIXTRACK tracking studies

6.3 Simulations and results

For the Dynamic aperture studies presented in the following a thin version of the FCC-hh lattice was used. In this version each triplet quadrupole is replaced by four thin quadrupoles. All other quadrupoles and dipoles in the lattice were replaced by two thin elements. At the time of the studies, the most recent version of the thin lattice contained the optimized lattice design from Chapter 5.3. Compared to following design, the triplet quadruple here are still unsplit and the assumed aperture was overestimated.

For the simulation, first a wide amplitude range was scanned with a larger amplitude step size. From the results the range was then narrowed down and the simulation were repeated with a smaller step size. The parameters used for the second iteration of the tracking studies can be found in Table 6.1.

The particles are initially distributed on a polar grid with the angles determined by

$$\theta_{N,i} = \frac{90° i}{N+1} \quad 1 \leq i \leq N \tag{6.5}$$

where N is the total number of angles. For every angle 30 particle pairs are distributed in an amplitude range of 2 σ. For the LHC, this parameters give an accuracy of the DA computation of about 0.5 σ [78].

The number of seeds accounts for 60 different realization of FCC-hh lattice with magnetic errors. This ensures that the lower bound of the DA is estimated with a 95 % confidence level [79].

It should be noted that only considering five angles can overestimated the DA by roughly 5% [80].

The magnetic field errors for the triplet quadrupoles were determined using the field quality table presented in [81]. The magnetic length of the straight part was adapted to the length of the triplet quadrupoles while the magnetic length of the ends was kept. The resulting field quality for triplet magnets is presented in Table 6.2 for Q1 and Q3

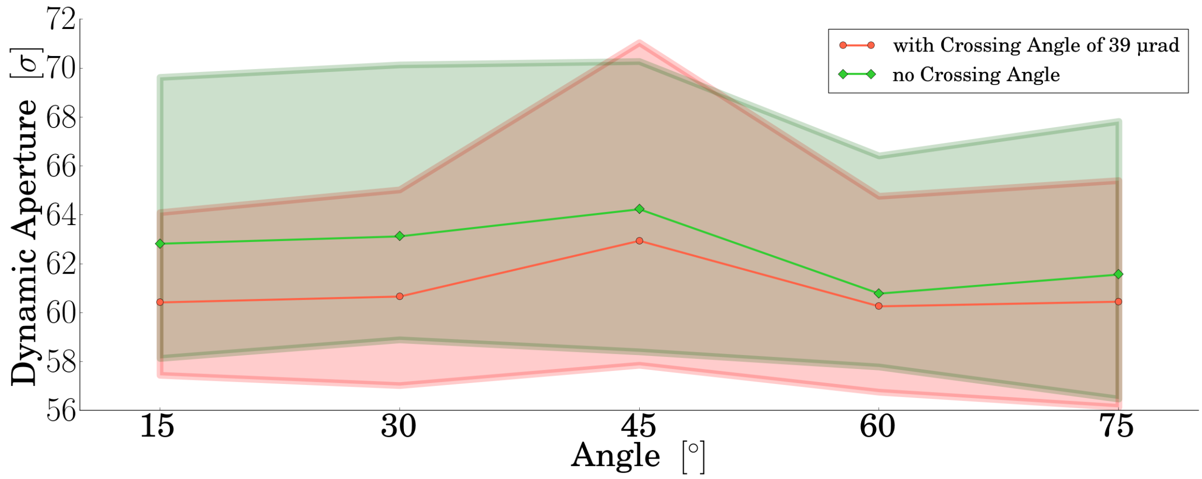

Figure 6.1: Dynamic aperture in the low luminosity insertion with and without crossing angle.

and in Table 6.3 for the quadrupoles Q2a and Q2b. The errors between the two types differ due to different lengths of the quadrupole types. In the simulations, dipolar and quadrupolar errors were not included. Furthermore, misalignments and tilts in the magnets were also not included in these first tracking studies.

The reference radius was scaled with the aperture from the initial 50 mm from the HL-LHC triplet to 22 mm for the triplet in the low luminosity experiments. Instead of using the overestimated coil aperture of 72 mm for this layout the corrected aperture of 64 mm from the later layout was used for scaling the reference radius. After the errors were assigned to the respective magnets, the tune and the chromaticity of the ring were rematched to the original values using the tune quadrupoles and sextupoles in the arcs.

The results with the above presented errors in the triplet quadrupoles in both low luminosity insertion are presented in Figure 6.1.

Both with and without the crossing angle the Dynamic aperture is well above the physical aperture of 15.5 σ indicating that no dedicating correction strategy of the magnet errors in the low luminosity insertion is required. The inclusion of the crossing angle reduces the minimum DA only by about 2 σ at most. The weak impact of the crossing angle is likely due to the small chosen crossing angle. It is expected that increasing the crossing angle will reduce the DA further due to increased feed-down effects. The DA for the most recent layout with split triplet quadrupoles is not expected to be significantly lower as magnet length and aperture did not change a lot and thereby the magnet errors will be similar.

The impact of the magnetic field errors in the low luminosity insertions on the DA when also considering errors in the high luminosity experiments was studied as well. The thin lattice used for this studies contained the $L^* = 45$m version of the high luminosity insertion [82]. The error table presented in [83] was used for the triplet magnets. The results, presented in Figure 6.2, indicate that the impact on the DA due to errors in the low luminosity insertions is mostly negligible except for the case of an angle of 60°.

	Systematic		**Uncertainty**		**Random**	
Normal	Injection	High Field	Injection	High Field	Injection	High Field
1	0	0	0	0	0	0
2	0	0	0	0	10	10
3	0	0	0.82	0.82	0.82	0.82
4	0	0	0.57	0.57	0.57	0.57
5	0	0	0.42	0.42	0.42	0.42
6	-20.332	-0.4379	1.1	1.1	1.1	1.1
7	0	0	0.19	0.19	0.19	0.19
8	0	0	0.13	0.13	0.13	0.13
9	0	0	0.07	0.07	0.07	0.07
10	3.728	-0.124	0.2	0.2	0.2	0.2
11	0	0	0.026	0.026	0.026	0.026
12	0	0	0.018	0.018	0.018	0.018
13	0	0	0.009	0.009	0.009	0.009
14	0.173	-0.867	0.023	0.023	0.023	0.023
15	0	0	0	0	0	0
Skew	Injection	High Field	Injection	High Field	Injection	High Field
1	0	0	0	0	0	0
2	-0.627	-0.627	0	0	10	10
3	0	0	0.65	0.65	0.65	0.65
4	0	0	0.65	0.65	0.65	0.65
5	0	0	0.43	0.43	0.43	0.43
6	0.044	0.044	0.31	0.31	0.31	0.31
7	0	0	0.19	0.19	0.19	0.19
8	0	0	0.11	0.11	0.11	0.11
9	0	0	0.08	0.08	0.08	0.08
10	0.002	0.002	0.04	0.04	0.04	0.04
11	0	0	0.026	0.026	0.026	0.026
12	0	0	0.014	0.014	0.014	0.014
13	0	0	0.01	0.01	0.01	0.01
14	-0.004	-0.004	0.005	0.005	0.005	0.005
15	0	0	0	0	0	0

Table 6.2: Normal and skew coefficients for Q1/Q3

	Systematic		Uncertainty		Random	
Normal	Injection	High Field	Injection	High Field	Injection	High Field
1	0	0	0	0	0	0
2	0	0	0	0	10	10
3	0	0	0.82	0.82	0.82	0.82
4	0	0	0.57	0.57	0.57	0.57
5	0	0	0.42	0.42	0.42	0.42
6	-19.918	-0.351	1.1	1.1	1.1	1.1
7	0	0	0.19	0.19	0.19	0.19
8	0	0	0.13	0.13	0.13	0.13
9	0	0	0.07	0.07	0.07	0.07
10	3.659	-0.130	0.2	0.2	0.2	0.2
11	0	0	0.026	0.026	0.026	0.026
12	0	0	0.018	0.018	0.018	0.018
13	0	0	0.009	0.009	0.009	0.009
14	0.157	-0.866	0.023	0.023	0.023	0.023
15	0	0	0	0	0	0
Skew	Injection	High Field	Injection	High Field	Injection	High Field
1	0	0	0	0	0	0
2	-0.895	-0.895	0	0	10	10
3	0	0	0.65	0.65	0.65	0.65
4	0	0	0.65	0.65	0.65	0.65
5	0	0	0.43	0.43	0.43	0.43
6	0.063	0.063	0.31	0.31	0.31	0.31
7	0	0	0.19	0.19	0.19	0.19
8	0	0	0.11	0.11	0.11	0.11
9	0	0	0.08	0.08	0.08	0.08
10	0.002	0.002	0.04	0.04	0.04	0.04
11	0	0	0.026	0.026	0.026	0.026
12	0	0	0.014	0.014	0.014	0.014
13	0	0	0.01	0.01	0.01	0.01
14	-0.006	-0.006	0.005	0.005	0.005	0.005
15	0	0	0	0	0	0

Table 6.3: Normal and skew coefficients for Q2

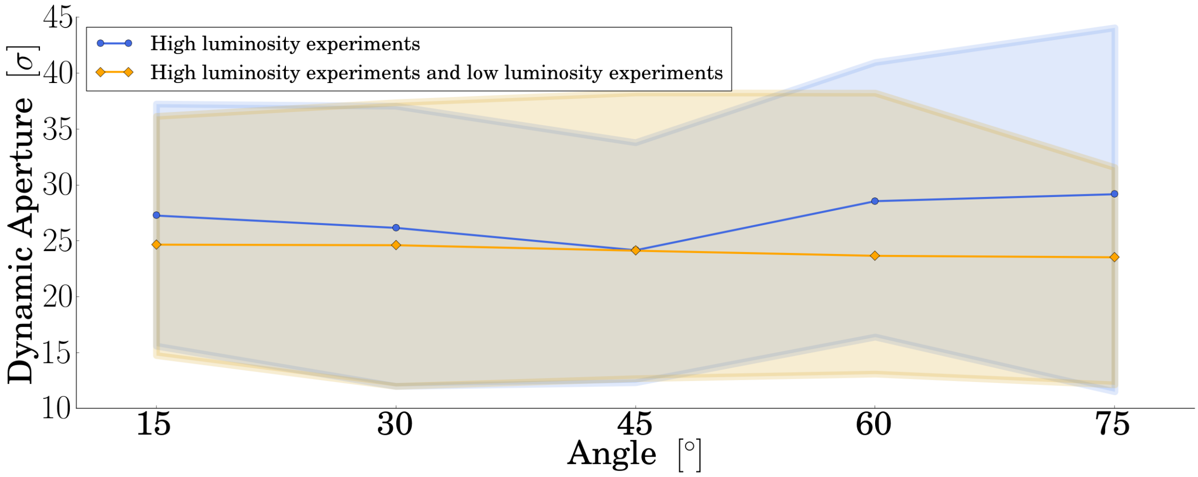

Figure 6.2: Dynamic aperture with error only in the high luminosity insertion and in both the high and low luminosity insertion without crossing angle.

Here the minimum DA is reduced by about 3σ.

Using crossing angles in both the high and the low luminsity experiments is going to reduce the DA even further. Tracking studies to investigate this were launched but for certain seeds, the TWISS module in MAD-X failed to find a solution. The reason for this is currently under investigation.

CHAPTER 7

Conclusion

The optics design of the experimental insertion in a particle collider plays a central role for the performance of the experiments. The achievable minimum beam size by the final focusing system determines the attainable luminosity, a key number for collider experiments.

In this thesis, a design for a combined experimental and injection was developed. Opting for a safe approach, the injection elements were placed as far away as possible from the experiments to mitigate the adverse effects of mis-injected beams on the experimental hardware. Taking into account the constraints from the injection hardware and magnet requirements the design is currently matched to allow for a β-function of 3 m in the interaction point. Together with the FCC-hh beam parameters, this allows to give a first number on the achievable instantaneous luminosity. Energy depositions studies with this design show, that the chosen shielding thickness in the triplet is sufficient in bringing the peak power density below the design limit. With the baseline FCC-hh target radiation limit, an estimate on the integrated luminosity can also be given.

The effects of magnetic field errors in the triplet quadrupoles on the Dynamic aperture at top energy were investigated. Using a first error table scaled for the large aperture quadrupoles in these insertions the tracking studies show a Dynamic aperture well above the physical aperture. Including the crossing angle in the low luminosity experiments results only in a slight reduction of the Dynamic aperture. The reduction of the Dynamic aperture in the presence of errors in the high luminosity experiments has also been studied and was found to be negligible.

In conclusion, the layout developed in this thesis should provide a stable basis for further layout iterations and for future beam stability studies.

Bibliography

[1] G. Aad *et al.*, “Observation of a new particle in the search for the Standard Model Higgs boson with the ATLAS detector at the LHC,” *Phys. Lett.*, vol. B716, pp. 1–29, 2012.

[2] S. Chatrchyan *et al.*, “Observation of a new boson at a mass of 125 GeV with the CMS experiment at the LHC,” *Phys. Lett.*, vol. B716, pp. 30–61, 2012.

[3] M. Aicheler, P. Burrows, M. Draper, T. Garvey, P. Lebrun, K. Peach, N. Phinney, H. Schmickler, D. Schulte, and N. Toge, “A Multi-TeV Linear Collider Based on CLIC Technology: CLIC Conceptual Design Report,” Tech. Rep. CERN-2012-007. SLAC-R-985. KEK-Report-2012-1. PSI-12-01. JAI-2012-001, Geneva, 2012.

[4] N. Phinney, N. Toge, and N. Walker, “ILC Reference Design Report Volume 3 - Accelerator,” Tech. Rep. arXiv:0712.2361, Dec 2007.

[5] “The European Strategy for Particle Physics Update 2013. 16th Session of European Strategy Council,” May 2013.

[6] O. S. Brüning, P. Collier, P. Lebrun, S. Myers, R. Ostojic, J. Poole, and P. Proudlock, *LHC Design Report*. CERN Yellow Reports: Monographs, Geneva: CERN, 2004.

[7] T. Kramer et al., “"Considerations for the Beam Dump System of a 100 TeV Centre-of-mass FCC hh Collider",” in *Proc. 6th International Particle Accelerator Conference, Richmond, VA, USA, paper TUPTY050, pp. 2132-2135*, 2015.

[8] M. Schaumann, “Ion Considerations.” `https://indico.cern.ch/event/556692/`

contributions/2484258/attachments/1467205/2268667/FCC_week_2017.pdf. presented at FCC week 2017, Berlin.

[9] J. Stanyard, Y. Loo, V. Mertens, J. Osborne, C. Sturzaker, and M. Sykes, "Optimisation of the Design of the Future Circular Collider from a Civil Engineering Perspective," in *Proc. of International Particle Accelerator Conference (IPAC'17), Copenhagen, Denmark, 14-19 May, 2017*, no. 8 in International Particle Accelerator Conference, (Geneva, Switzerland), pp. 2392–2394, JACoW, May 2017. https://doi.org/10.18429/JACoW-IPAC2017-TUPVA127.

[10] A. Chancé, D. Boutin, B. Dalena, B. Holzer, A. Langner, and D. Schulte, "Updates on the Optics of the Future Hadron-Hadron Collider FCC-hh," in *Proc. of International Particle Accelerator Conference (IPAC'17), Copenhagen, Denmark, 14-19 May, 2017*, no. 8 in International Particle Accelerator Conference, (Geneva, Switzerland), pp. 2023–2026, JACoW, May 2017. https://doi.org/10.18429/JACoW-IPAC2017-TUPVA002.

[11] D. Schulte, "Preliminary Collider Baseline Parameters: Deliverable D1.1," Tech. Rep. CERN-ACC-2015-0132, CERN, Geneva, Sep 2015.

[12] F. Zimmermann, "HE-LHC baseline parameters." https://indico.cern.ch/event/556692/contributions/2590826/attachments/1469360/2272924/HE-LHC-Baseline-Parameters.pdf. presented at FCC week 2017, Berlin.

[13] O. Brüning, J. Jowett, M. Klein, D. Pellegrini, D. Schulte, and F. Zimmermann, "Future Circular Collider Study FCC-he Baseline Parameters," Tech. Rep. CERN-ACC-2017-0019, CERN, Geneva, Apr 2017.

[14] M. Bicer et al., "First Look at the Physics Case of TLEP. First Look at the Physics Case of the FCC-ee (TLEP)," *JHEP*, vol. 01, p. 164. 50 p, Aug 2013.

[15] M. Benedikt and F. Zimmermann, "Status and Challenges of the Future Circular Collider Study," Tech. Rep. CERN-ACC-2016-0005, CERN, Geneva, Jan 2016.

[16] M. Reiser, *Theory and design of charged particle beams; 2nd ed.* Weinheim: Wiley, 2008.

[17] H. Wiedemann, *Particle accelerator physics; 4th ed.* Berlin: Springer, 2015.

[18] P. J. Bryant and K. Johnsen, *The Principles of Circular Accelerators and Storage Rings*. Cambridge: Cambridge Univ. Press, 1993.

[19] K. Wille, *The physics of particle accelerators: an introduction*. Oxford: Oxford Univ. Press, 2000.

[20] CMS Collaboration, *CMS Physics: Technical Design Report Volume 1: Detector Performance and Software*. Technical Design Report CMS, Geneva: CERN, 2006.

[21] S. White, "Luminosity Scans at the LHC. Luminosity Scans at LHC," 2011.

[22] P. D. Hermes, J. Jowett, and J. P. Wessels, "Development of high β^*-optics for ALICE," Apr 2013. Presented 31 May 2013.

[23] "SAD - Strategic Accelerator Design." `http://acc-physics.kek.jp/SAD/`. Accessed: 10.08.2017.

[24] "MAD-X - Methodical Accelerator Design." `https://madx.web.cern.ch/madx/`. Accessed: 10.08.2017.

[25] "MAD-X - User Guide." `http://madx.web.cern.ch/madx/releases/last-dev/madxuguide.pdf`. Accessed: 10.08.2017.

[26] F. Schmidt, E. Forest, and E. McIntosh, "Introduction to the polymorphic tracking code: Fibre bundles, polymorphic Taylor types and "Exact tracking"," Tech. Rep. CERN-SL-2002-044-AP. KEK-REPORT-2002-3, CERN, Geneva, Jul 2002.

[27] "Sixtrack - 6D Tracking Code." `http://sixtrack.web.cern.ch/SixTrack/`. Accessed: 10.08.2017.

[28] "LHC@Home." `https://lhcathome.cern.ch/lhcathome/`. Accessed: 10.08.2017.

[29] E. D. Courant, M. S. Livingston, H. S. Snyder, and J. P. Blewett, "Origin of the "strong-focusing" principle," *Phys. Rev.*, vol. 91, pp. 202–203, Jul 1953.

[30] E. D. Courant, M. S. Livingston, and H. S. Snyder, "The strong-focusing synchroton—a new high energy accelerator," *Phys. Rev.*, vol. 88, pp. 1190–1196, Dec 1952.

[31] W. Herr and B. Muratori, "Concept of luminosity," 2006.

[32] O. Brüning, H. Burkhardt, and S. Myers, "The Large Hadron Collider," *Prog. Part. Nucl. Phys.*, vol. 67, pp. 705–734. mult. p, Apr 2012.

[33] O. S. Brüning and S. D. Fartoukh, "Field Quality Specification for the LHC Main Dipole Magnets," Tech. Rep. LHC-Project-Report-501. CERN-LHC-Project-Report-501, CERN, Geneva, Oct 2001.

[34] E. Todesco and F. Savary, "HL-LHC Magnet Roadmap," 2015.

[35] CERN, *CAS - CERN Accelerator School: Advanced Accelerator Physics Course*, (Geneva), CERN, 2014. CERN Accelerator School in collaboration with The Norwegian University of Science and Technology (NTNU).

[36] C. Bracco, "Injection: Hadron beams." `https://indico.cern.ch/event/451905/contributions/2159032/attachments/1425216/2188137/CAS_ERICE_Hadrons_Injection.pdf`. presented at CAS, Erice 2017.

[37] M. Paraliev, "Septa." `https://indico.cern.ch/event/451905/contributions/2159074/attachments/1421967/2194202/Septa_II.pdf`. presented at CAS, Erice 2017.

[38] M. Barnes, "Kicker magnets." `https://indico.cern.ch/event/451905/contributions/2159055/attachments/1424705/2191232/BARNES_CAS_Mar17_Kickers-PtA.pdf`. presented at CAS, Erice 2017.

[39] M. Fraser, "Single and multi-turn extraction." `https://indico.cern.ch/event/451905/contributions/2159062/attachments/1424164/2204353/CAS_ABT_Extraction_Erice_v5.pdf`. presented at CAS, Erice 2017.

[40] O. S. Brüning, "Optics Solutions for the Combined Experimental and Injection Regions in the LHC," p. 4 p, Jun 1998.

[41] J. B. Jeanneret and T. Risselada, “Geometrical Aperture in LHC at Injection,” Tech. Rep. LHC-Project-Note-66, CERN, Geneva, Sep 1996.

[42] C. Garion, “FCC-hh Beam screen studies and beam screen cooling scenarios.” https://indico.cern.ch/event/438866/contributions/1084911/attachments/1257787/1857527/Beam_screen_studies.pdf. presented at FCC Week 2016, Rome.

[43] A. Ferrari, P. R. Sala, A. Fassò, and J. Ranft, *FLUKA: A multi-particle transport code (program version 2005).* CERN Yellow Reports: Monographs, Geneva: CERN, 2005.

[44] T.T. Böhlen, F. Cerutti, M.P.W. Chin, A. Fassò, A. Ferrari, P.G. Ortega, A. Mairani, P.R. Sala, G. Smirnov and V. Vlachoudis, “"The FLUKA Code: Developments and Challenges for High Energy and Medical Applications".” Nuclear Data Sheets 120, 211-214 (2014).

[45] S. Roesler, R. Engel, and J. Ranft, “The Monte Carlo Event Generator DPMJET-III,” Tech. Rep. hep-ph/0012252. SLAC-PUB-8740, SLAC, Stanford, CA, Dec 2000.

[46] S. Fartoukh et al., “LHC triplet lifetime versus operational scenario in ATLAS and CMS.” https://indico.cern.ch/event/406858/contributions/966580/attachments/813759/1115141/LMC_IR1sign.pdf. presented at 225th LHC Machine Committee.

[47] R. Martin, M. I. Besana, F. Cerutti, A. Langner, R. Tomás, E. Cruz-Alaniz, and B. Dalena, “Interaction region design driven by energy deposition,” *Phys. Rev. Accel. Beams*, 2017. Accepted for Publication.

[48] W. Herr, “Effects of PACMAN bunches in the LHC,” Tech. Rep. LHC-Project-Report-39. CERN-LHC-Project-Report-39, CERN, Geneva, Jul 1996.

[49] B. Dalena, “Layout and arc lattice design.” https://indico.cern.ch/event/340703/contributions/802144/attachments/668729/919185/bdalena_fcc_week_2015.pdf. presented at FCC Week 2015, Washington.

[50] J. Stanyard, “FCC Civil Engineering Optimisation and Design Development.” https://indico.cern.ch/event/556692/contributions/2496900/

attachments/1468800/2271843/Civil_Engineering_Optimisation_and_Design_Development.pdf. presented at FCC Week 2017, Berlin.

[51] A. Lechner, A. Alnuaimi, C. Bracco, F. Cerutti, A. Christov, L. S. Esposito, N. V. Shetty, and V. Vlachoudis, "Energy Deposition Studies for Fast Losses during LHC Injection Failures," in *Proceedings, 4th International Particle Accelerator Conference (IPAC 2013): Shanghai, China, May 12-17, 2013*, p. TUPFI027, 2013.

[52] CERN, *3rd Evian Workshop on LHC beam operation*, (Geneva), CERN, 2011.

[53] G. Apollinari, I. Béjar Alonso, O. Brüning, M. Lamont, and L. Rossi, *High-Luminosity Large Hadron Collider (HL-LHC): Preliminary Design Report*. CERN Yellow Reports: Monographs, Geneva: CERN, 2015.

[54] F. Burkart, "scSPS as 1.3 TeV HEB." https://indico.cern.ch/event/556692/contributions/2484267/attachments/1467209/2268675/scSPS_FCCweek2017_FB.pdf. presented at FCC Week 2017, Berlin.

[55] W. Riegler, "private communication." 2016.

[56] E. Todesco, "Magnet specifications and targets." https://indico.cern.ch/event/340703/contributions/802084/attachments/668672/919093/et_fcc_1503.pdf. presented at FCC Week 2015, Washington.

[57] F. Burkart, "private communication." 2016.

[58] A. Chancé, D. Boutin, B. Dalena, B. Holzer, R. Martin, J. Payet, and D. Schulte, "Status of the Beam Optics of the Future Hadron-Hadron Collider FCC-hh," in *Proceedings, 7th International Particle Accelerator Conference (IPAC 2016): Busan, Korea, May 8-13, 2016*, p. TUPMW020, 2016.

[59] M. Fiascaris, R. Bruce, D. Mirarchi, and S. Redaelli, "First Design of a Proton Collimation System for 50 TeV FCC-hh," no. CERN-ACC-2016-221, p. WEPMW006. 4 p, 2016.

[60] R. Bruce et al., "Updated parameters for hl-lhc aperture calculations for proton beams," Tech. Rep. CERN-ACC-2017-0051, CERN, Geneva, Jul 2017.

[61] R. Martin, R. Tomás, and B. Dalena, "Interaction Region for a 100 TeV Proton-Proton Collider," no. IPAC-2015-TUPTY001. CERN-ACC-2015-365, p. TUPTY001. 4 p, 2015.

[62] M. Fiascaris, "Collimation Status." `https://indico.cern.ch/event/567230/contributions/2346535/attachments/1367781/2072805/EuroCirCol_Nov2016_CollimationOverview.pdf`. Accessed: 19.08.2017.

[63] M. I. Besana, "private communication." 2017.

[64] "FCC-hh lattice model." `https://gitlab.cern.ch/fcc-optics/FCC-hh-lattice`.

[65] D. Schörling, "private communication." 2017.

[66] L. Bottura, "Magnets - highlights and a summary." `https://indico.cern.ch/event/556692/contributions/2487576/attachments/1469807/2274048/summary_magnets.pdf`. presented at FCC Week 2017, Berlin.

[67] A. S. Langner, "Betatron collimation system insertions." `https://indico.cern.ch/event/556692/contributions/2484254/attachments/1467177/2268615/talk_alangner.pdf`. presented at FCC Week 2017, Berlin.

[68] A. S. Langner, "private communication." 2017.

[69] M. Ferro-Luzzi, W. Herr, and T. Pieloni, "LHC bunch filling schemes for commissioning and initial luminosity optimization," Tech. Rep. LHC-Project-Note-415. CERN-LHC-Project-Note-415, CERN, Geneva, Jun 2008.

[70] J. M. Jowett, "Collision Schedules and Bunch Filling Schemes in the LHC," Tech. Rep. LHC-PROJECT-NOTE-179, CERN, Geneva, Feb 1999.

[71] D. Schulte, "Parameter and layout." `https://indico.cern.ch/event/556692/contributions/2484245/attachments/1467275/2268803/Berlin_layout2.pdf`. presented at FCC Week 2017, Berlin.

[72] D. Schörling, "Impact of irradiation on margins of high-luminosity ir triplet magnets." `https://indico.cern.ch/event/647002/contributions/2628508/`

attachments/1481855/2298501/Schoerling_RadiationLimits.pdf. presented at the first FCC-hh other magnet design meeting, on June, 23th ,2017.

[73] T. Pieloni, "Beam-beam studies for FCC-hh." https://indico.cern.ch/event/556692/contributions/2484262/attachments/1467450/2270723/FCCBerlin2017_Pieloni.pdf. presented at FCC Week 2017, Berlin.

[74] L. V. Riesen-Haupt, "First overview of the magnets for an alternative high luminosity irs." https://indico.cern.ch/event/589686/contributions/2484803/attachments/1429322/2194827/Alternative_Flat_Beam_Triplet.pdf. presented at the first FCC-hh magnet-beam dynamics coordination meeting meeting, on March, 17th ,2017.

[75] M. Giovannozzi, W. Scandale, and E. Todesco, "Prediction of Long-Term Stability in Large Hadron Colliders," *Part. Accel.*, vol. 56, pp. 195–225. 32 p, Jul 1996.

[76] "CAS: Fifth advanced accelerator physics school." http://cds.cern.ch/record/254747/files/CERN-95-06-V1-V2.pdf?version=2.

[77] R. Wolf, "Field Error Naming Conventions for LHC Magnets." LHC-M-ES-0001 rev 3.0, EDMS no. 90250.

[78] M. Hayes, E. McIntosh, and F. Schmidt, "The Influence of Computer Errors on Dynamic Aperture Results Using SixTrack," Tech. Rep. LHC-PROJECT-NOTE-309, CERN, Geneva, Jan 2003.

[79] J.-P. Koutchouk, M. Böge, A. Faus-Golfe, J. Gareyte, H. Grote, J. Miles, Q. Qing, T. Risselada, F. Schmidt, and S. Weisz, "Overview of the LHC dynamic aperture studies," p. 3 p, Jun 1997.

[80] M. Giovannozzi and E. McIntosh, "Parameter scans and accuracy estimates of the dynamical aperture of the CERN LHC," p. 4 p, Jul 2006.

[81] E. Todesco et. al, "Insertion magnets, HL-LHC PDR." CERN-ACC-2014-103 (2015).

[82] A. Seryi *et al.*, "Overview of Design Development of FCC-hh Experimental Interaction Regions," in *Proc. of International Particle Accelerator Conference (IPAC'17), Copenhagen, Denmark, 14-19 May, 2017*, no. 8 in International Particle Accelerator Conference, (Geneva, Switzerland), pp. 2151–2154, JACoW, May 2017. https://doi.org/10.18429/JACoW-IPAC2017-TUPVA040.

[83] R. Martin, "$\beta^* - reach\ studies$." `https://indico.cern.ch/event/438866/contributions/1085157/`. presented at FCC Week 2016, Rome.